Nanoscale digital image correlation at elementary fibre/matrix level in polymer–based composites

Nathan Klavzer[a,*] and Sarah Gayot[a,b], Michaël Coulombier[a], Bernard Nysten[b] and Thomas Pardoen[a]

[a] Institute of Mechanics, Materials and Civil engineering (iMMC), UCLouvain, B-1348 Louvain-la-Neuve, Belgium
[b] Institute of Condensed Matter and Nanosciences (IMCN), UCLouvain, B-1348 Louvain-la-Neuve, Belgium
*corresponding author

Email addresses: nathan.klavzer@uclouvain.be (N. Klavzer), sarah.gayot@uclouvain.be (S. Gayot), michael.coulombier@uclouvain.be (M. Coulombier), bernard.nysten@uclouvain.be (B. Nysten), thomas.pardoen@uclouvain.be (T. Pardoen).

Abstract

Multiscale mechanical modelling aims at predicting the failure of composites from the fibre/matrix level up to the component scale. Existing frameworks are limited by the lack of reliable experimental data and by an incomplete understanding of the submicron deformation and failure mechanisms. A novel digital image correlation (DIC) method has been developed for the characterisation of the nanoscale mechanical response in composites, based on latest advances in surface patterning. Indium has been deposited on unidirectional composites leading to a dense, homogeneous speckle with particle diameter around 15 nm. The specimens were subjected to transverse compression in a scanning electron microscope, while minimising distortion effects. Strain concentration areas, like submicron shear bands and fibre-matrix interphases, were successfully captured for two systems: a carbon fibre-reinforced thermoset and a glass fibre-reinforced thermoplastic. DIC results were compared with alternative experimental data, obtained by atomic force microscopy, and with finite element simulations based on a conventional elastoplastic model.

Keywords: *Digital Image Correlation (DIC), Polymer-matrix composites (PMCs), Micro-mechanics, Interface/interphase*

1. Introduction

Quantitative submicron scale experimental data about the deformation and failure of fibre-reinforced polymer composites (FRP) at the matrix/interface/fibre level is currently missing, preventing a full understanding of the local mechanics and impeding the development of enriched micromechanical models. Bottom-up multiscale mechanics approaches are indeed at the core of the advanced design strategy of fail-safe composite structures [1]. Available finite element (FE) numerical frameworks rely on experimental results for modelling the behaviour of FRPs at the micro- (ply level), meso- (laminate level) and macro- (part level) scales [2]. While macro- and mesoscale properties are relatively straightforward to extract using classical mechanical tests, the response at the microscale has yet to be fully explored especially in terms of quantitative mechanical behaviour data. Evidence shows that neglecting the local fibre/matrix behaviour, such as possible size effects, the presence of an interphase of different nature, local variations in polymer structure and/or constraint effects on local shear banding, significantly limits the accuracy of numerical predictions, particularly in loading conditions where the matrix is the main carrier of deformation (i.e. transverse compression or shear) [3]. In other words, one cannot 'simply' rely on the bulk polymer mechanical response and known fibre behaviour to model the microlevel.

A number of experimental approaches are available to address the local matrix, fibre-matrix interface and interphase characterisation, see recent review [4]. Nanoindentation has been widely used to characterise both bulk polymer glasses and 'confined' matrices within FRPs [5–11]. Although the interpretation of experimental load-penetration curves in small matrix pockets remains controversial, the properties determined by nanoindentation very often differ from those extracted from macroscale tests. The local strength in FRPs tends to be 15-20% higher compared to bulk samples, while stiffness is also often found to be larger within inter-fibre matrix regions. Nanoindentation data have been used to either determine the underlying deformation mechanisms or to feed FE models [12]. Atomic force microscopy (AFM) has been applied to FRPs to determine local heterogeneities and to map the size of the interphase region around the fibres. The local property landscape in polymer glasses is systematically heterogeneous and the size of the interphase is found to be ranging from a few tens of nanometres up to a few microns [13–16]. However, nanoindentation and AFM do not provide information on the stress and strain fields during loading.

Recently, micro digital image correlation (DIC) has been adapted to the study of FRPs, aiming at characterising the local deformation processes [17,18]. DIC is a non-contact method, which tracks the

relative displacement of material points between two images. The strain field is then extracted from the displacement field [19,20]. DIC can, in theory, be applied at any scale as long as a suitable speckle pattern (i.e. used for the tracking) can be created or by using inherent material surface features. Although macro DIC is widely used by the composite community [21–23], the use of micro DIC remains scarce and nano DIC has, to the authors' knowledge, not been applied to FRPs yet.

Micro DIC on FRPs was first introduced by Canal et al. [17]. In-situ transverse compression tests were performed within a scanning electron microscope (SEM) on unidirectional (UD) composite samples to favour matrix plasticity. A fine alumina dispersion was used to track displacements. The potential of micro DIC was demonstrated by qualitatively mapping the strain fields over the region of interest (ROI), in accordance with FEA predictions. Inter-fibre strain localisation was also detected, however the overall strain measurements for each phase were inaccurate due to averaging by the correlation algorithm linked to speckle coarseness. Subsequent studies by Mehdikhani et al. [18,24] showed that micro DIC is also capable of clearly identifying regions of strain concentration or even the presence of carbon nanotube clusters. Yet, the authors pointed out the importance of evaluating the error resulting from the speckle pattern quality, DIC analysis parameters and SEM-related effects (e.g. charging, spatial and drift distortion, etc.). Hence, the speckle pattern quality is the primary factor limiting the quantitative use of micro DIC at the fibre/matrix level. More recently, Chevalier et al. [3] performed an extensive experimental and numerical study on the transverse compression of UD specimens. The DIC maps did not match the FE predictions obtained with a classical continuum model in confined regions between fibres, where the FEA largely overestimates the strain amplitude. The key conclusions from these studies are, on the one hand, that the accuracy of micro DIC is mainly limited by the speckle pattern quality and SEM artefacts and, on the other hand, that macroscale continuum models are unable to quantitatively capture microscale deformation behaviours in confined volumes.

In order to extract quantitative information from micro DIC, issues related to the speckle pattern and SEM have to be addressed. Improving the speckle pattern quality has been a point of interest for many material systems [25–27]. The goal is to obtain a high contrast and dense speckle pattern with a submicron speckle size, which significantly increases the spatial resolution of the DIC analysis. Hoefnagels et al. [28] recently proposed a novel approach allowing for a resolution of a few tens of nanometres, hence justifying the use of the "nano DIC" terminology. The method relies on the ability of some metals to create thin films from the nucleation, growth and coalescence of nanometric clusters or

'islands' (Volmer-Weber growth mode). This particular growth mode is observed when adatoms have a high diffusion length on the substrate surface, which may be achieved by depositing a metal (or alloy) with a low melting temperature, while providing high kinetic energy to the deposited atoms via low-pressure deposition methods, e.g. physical vapour deposition (PVD) [28,29]. Hoefnagels et al. showed that the physical vapour deposition of certain indium-based solder alloys by magnetron sputtering yields the formation of speckle patterns with controlled morphologies (i.e. particle shape, size, and density) on metallic substrates, without requiring substrate heating. This method was used successfully to quantify strain localisation – and thus predict failure location - in polycrystalline iron foils [28].

Nevertheless, a high-resolution speckle is not sufficient to guarantee the overall spatial resolution of DIC measurements, which also depends on the accuracy of the imaging technique. In the case of in-situ mechanical tests performed in a SEM chamber, so-called image distortions – i.e. deviations with respect to the 'ideal' image positions [30] - can occur and eventually give rise to spurious displacements and thus invalid strains extraction. SEM-related distortions may be separated into space- and time-dependent effects, as proposed by Sutton et al. [30,31] and other subsequent studies [32–34]. Spatial distortions (e.g. due to lens aberrations) do not evolve over time, unlike temporal or 'drift' distortions. The latter may arise from the components making up the SEM or even charging of the imaged material. Positioning errors of the electron beam during scanning, referred to as 'scan line shifts' [27,30,33], may also fall under this category, but the impact on DIC measurements has not been extensively studied in the literature – probably because they give rise to highly recognisable line patterns on DIC strain maps.

Spatial distortions have been shown to remain relatively constant throughout a given experiment and to be more prevalent at low magnifications, meaning that the effect on micro or nano DIC should be limited [35]. Drift distortions, however, are more significant at high magnifications, and can induce large overestimations in the measured displacements. Several methods have been proposed to correct for drift distortions, but the simplest approach consists in taking pairs of images at each step during in-situ testing and evaluating the relative shift between them [35]. When the material presents strong stress relaxation, as in polymer glasses, accounting for the effect of stress relaxation on the drift is key and can lead to degraded DIC measurements if not properly dealt with [35]. An alternative approach is to improve the correlation algorithm to take into account such artefacts, as done in [32,34].

In this study, we combine the latest advances in patterning techniques for micro and nano DIC with in-situ transverse compressions on UD FRPs in order to reveal, for the first time, fine details of the local

deformation and failure of the constituents at the fibre/matrix level. This application of nano DIC on FRPs has been made possible by adapting the speckle deposition technique developed by Hoefnagels et al. [28]. Here, we simplify the approach by using electron beam (e-beam) evaporation of pure indium, where only the deposition time (and hence the particle size) can be controlled. The resulting dense and homogeneous nanoscale pattern exhibits particle sizes ranging from 10 nm to a few hundred nm. This pattern is applied to two types of FRPs: a glass fibre-reinforced thermoplastic and a carbon fibre-reinforced thermoset. It allows overcoming the main challenge of low-scale DIC on FRPs, which is the accurate separation of the displacements and strains in each of the constituents. In particular, the size of the matrix-modified interphase region around the fibres can be measured, which was impossible so far due to the averaging within the DIC algorithm linked to an insufficiently fine speckle pattern. The methodology adopted to minimise the impact of SEM-related distortions is also presented in this paper. The results are compared first to AFM data and then to FE predictions made using a continuum model with pre-identified parameters for the matrix.

2. Materials and Experimental Methods

2.1 Manufacturing of composite specimens

Glass fibre-reinforced thermoplastic composites

UD glass fibre-reinforced thermoplastic (TP) composite samples were provided by Arkema (France). The thermoplastic matrix comprised a pultrusion-grade methyl methacrylate-based monomer formula, Elium® 591 (Arkema), and 1 part per hundred ratio of the following peroxide thermal initiators: Perkadox® 16 (Nouryon, the Netherlands), Trigonox® 141 (Nouryon) and Luperox® DEC (Arkema). 2400-tex SE 4740 glass rovings (3B-The Fiberglass Company, Belgium) were used as reinforcement. Continuous unidirectional composite profiles with a final thickness equal to 2 mm and fibre volume fraction (V_f) close to 65% were produced by pultrusion. Parallelepipedic specimens of dimensions 4×2×3 mm³ were machined using a water-cooled disc milling cutter, as shown in Figure 1 (a). The choice of specimen geometry and dimensions was driven by two factors: (1) the limitation associated to the 2 mm-thick UD composite samples manufactured industrially by Arkema and (2) the features of the compression stage and SEM chamber used for in-situ testing, see section 2.3. More precisely, the *z*-dimension was matched with the groove depth of compression jaws (i.e. 3 mm) to optimize electric contact with the metal and

minimize working distance during SEM imaging. Additionally, the strength of the specimen had to remain below the load limit of the compression stage, i.e. 2 kN.

Carbon fibre-reinforced thermoset composites

A UD carbon fibre-reinforced thermoset (TS) composite plate was produced by resin transfer moulding according to the procedure described in [3], using the monocomponent HexFlow RTM6 resin from Hexcel (CT, USA) and HTS 12k carbon fibres (Saertex Gmbh, Germany). The final V_f value was close to 40%. Parallelepipeds of dimensions 5×5×3 mm³ were machined using a water-cooled disc milling cutter, and two notches were drilled parallel to fibre orientation as shown in Figure 1 (b). In this case, specimen geometry and dimensions had already been determined by Chevalier et al. [3] so as to remain within the limits of the compression stage load cell (see section 2.3) and induce stress concentration during testing.

Note that different geometries and fibre volume fractions were used for the carbon fibre-reinforced TS and the glass fibre-reinforced TP transverse compression specimens, for the practical reasons mentioned above. However, this should not compromise the comparability of DIC measurements between the two systems, as the nature of nanoscale plastic deformation and failure phenomena occurring between fibres in a given system depends mostly on the local fibre arrangement within the ROI (i.e. inter-fibre distance, fibre diameter and orientation of the inter-fibre matrix strip with respect to the unidirectionally-applied load).

Polishing of composite surfaces

Both types of composite specimens were polished perpendicular to fibre orientation (i.e. *z*-axis) on a semi-automatic MultiPrep Precision Polishing System (Allied High Tech Products, Inc., CA, USA). Resin-bonded diamond discs with successive grit of 1200 and 4000 (MD-Piano from Struers Inc., OH, USA) were used for grinding, while finishing was performed with a 0.3-µm alumina suspension (AP-D Suspension 0.3 µm, Struers Inc.).

2.2 Speckle pattern deposition

The protocol developed by Hoefnagels et al. [28] for depositing nanometric DIC speckles onto metallic specimens by PVD was simplified and applied to polymer composite substrates as follows. Indium deposition was performed by e-beam evaporation, using indium pellets with a purity of 99.99%. The deposition rate was kept equal to 1 Å.s^{-1} and the operating pressure never exceeded 4×10^{-7} mbar. The

influence of the deposition time on speckle pattern morphology was assessed using silicon wafers as the substrate material. More precisely, several deposition times were tested, in order to produce the following target coating thicknesses: 2 nm, 5 nm, 10 nm, 20 nm and 50 nm. The results of this preliminary study are presented in section 3.1. Note that indium was selected among the list of commonly evaporated materials for several reasons. First, pure indium has a low melting point under standard temperature and pressure conditions (around 157 °C [36]), which should favour the formation of metal 'islands' on the substrate material instead of a continuous film during PVD, as mentioned previously [28]. It is also chemically inert to air and water under ambient conditions, which guarantees the stability of the coating between the deposition and imaging steps. Metallic indium is easily available and relatively inexpensive compared to other metals used for e-beam evaporation [37]. Last, human toxicity of metallic indium is low under occupational conditions [38].

2.3 SEM imaging and in-situ compression testing

Imaging of indium-coated Si wafers

An Ultra 55 Field-Emission SEM (Zeiss, Germany) was used for imaging the indium speckle patterns deposited onto Si wafers, see section 3.1. The acquisition parameters were similar to those applied during the in-situ compression testing of composite specimens, see below.

Preparation of composite specimens for SEM imaging and mounting on compression stage

Unwanted charging effects arise when poor electric conductors, like polymer composites, are imaged by SEM. As detailed in section 2.4, charging may be detrimental to image quality (especially at high magnifications) and can ultimately lead to surface degradation, impacting in turn the accuracy of DIC measurements. Following indium deposition, polished composite surfaces were therefore subjected to carbon sputtering, and all other free surfaces were coated with a thin layer of silver lacquer. Composite specimens were mounted on a microtest compression stage equipped with a 2 kN load cell (Deben UK Ltd., UK) and further placed inside the chamber of an Ultra 55 Field-Emission SEM (Zeiss, Germany). Figure 2 shows the experimental setup ready for insertion in the SEM.

Compression testing and acquisition of DIC data

For each specimen, one or two zones of interest were selected for DIC measurements and imaged with both a 5.7×4.3 µm² and 11.4×8.6 µm² field of view (i.e. at a magnification of 20,000 and 10,000 in our

case), and a pixel size close to 6 and 12 nm, respectively. Acceleration voltage was kept in the 2-4 keV range to limit charging effects. When needed, contrast and brightness values were adapted during the test in order to counter the progressive darkening of SEM images induced by remaining charging effects.

Each region of interest (ROI) was imaged before and during uniaxial compression along the *x*-axis. Loading was performed using 50 to 100 N increments, in between which the stage motor was stopped. SEM images were taken at each load increment after the specimen was left to relax until the load drop over a two-minute period (i.e. average time to take two successive SEM images) was less than 1 N (see section 2.4 for further details). Compression was continued until macroscopic fracture of the specimen.

2.4 DIC data processing

Image analysis

The size distribution of indium particles deposited on silicon wafers and composite specimens was assessed using the open-source software ImageJ. SEM images were subjected to binary thresholding, and a watershed segmentation algorithm was applied to separate any spuriously connected particles. The built-in particle analysis tool of ImageJ was run, and the resulting data were processed with Matlab (R2021b). A sample size of at least 1,000 particles was used for each case.

DIC measurements

The DIC analyses were carried out using the open-source software Ncorr [39], which relies on three input parameters: the subset size, step size and strain radius value. The 'subset' refers to a group of pixels in which strains are assumed to be homogeneous, while the 'step' denotes the spatial shift between two adjacent subsets. The value of the strain radius indicates the size of the smoothing filter applied when converting displacement fields into strain fields. Note that the choices of subset and step size condition the spatial resolution of calculated displacements, while that of strain radius impacts the level of numerical noise in the final strain maps. The systematic approach of Mehdikhani et al. [18] was followed in order to find a suitable combination of input parameters with respect to (1) the morphology of the speckle pattern and (2) the quality of the SEM images obtained in this work. More precisely, a well-speckled zone of an undeformed TP composite specimen was imaged by SEM at the magnification levels of interest for DIC, i.e. 10,000 and 20,000. The images, of respective dimensions 991×673 px² and 828×612 px², were then numerically stretched by 10 px in the *x*-direction using the lanczos3 tool of Matlab (R2021b). The extracted uniaxial strains ε_{xx} were close to the expected values of 0.0101 and

0.0121, respectively. For both levels of magnification, DIC measurements were performed between the original and stretched SEM images, with different sets of subset size, step size and strain radius values. The values obtained by DIC for the mean strain (and corresponding standard deviation) were compared to the theoretical values of ε_{xx} mentioned above. The results of the strain deviation analysis are presented in section 3.1.

As mentioned in the introduction, SEM imaging induces spatial and drift (i.e. temporal) distortions. Kammers et al. [35] proposed a straightforward method for addressing both types of artefacts without modifying the DIC algorithm. First, to correct spatial distortions for each sample, a series of four overlapping images in the horizontal (u) and four images in the vertical (v) directions are taken over a defined distance. In addition, at each displacement increment, a pair of images is taken to correct for drift distortions (i.e. see below). The total applied displacement increment should be selected so that the total displacement in each direction does not exceed ¼ of the field of view of the DIC analyses. However, the smallest possible translation within this study was limited to 1 µm due to the SEM stage accuracy limitations. Since the imposed displacement is known (from the rigid body motion principle), it can be subtracted from the calculated displacement fields, resulting in so-called 'spatial distortion maps'. A linear relationship relating the amplitude of the distortion in the u and v directions and the imposed translation is extracted from the results. This function may be used as a correction tool for spatial distortions, which takes, as input, the u and v displacements at each point of the DIC fields. Second, drift distortions can be measured by taking two consecutive images at each load increment. For each pair of SEM scans, the calculated DIC maps are subtracted from one another. The resulting difference in displacement amplitude over the ROI determines the error related to drift distortions. The horizontal and vertical displacement drift maps are then subtracted from the actual DIC displacement maps to get drift-free maps. Finally, the impact of stress relaxation was determined on the two consecutive images used for drift correction. The evolution of the load as a function of time was monitored during image acquisition. Hence, each pixel may be related to its acquisition time and the corresponding load value, resulting in so-called 'load maps'. In this study, the composite specimens were systematically left to relax in between load increments, so that the load drop never exceeded 1 N during the acquisition of two consecutive images. The corresponding error on DIC strain measurements was found to be negligible, as shown in Figure 20 in the Appendix.

2.5 Atomic force microscopy

Micromechanical analysis of the Elium and RTM6 composite systems by AFM was performed on Dimension Icon and MultiMode 8 systems (both from Bruker Corp., USA), using PeakForce Tapping®-QNM mode [40] and a factory-calibrated RTESPA-300-30 probe (Bruker). The cantilever spring constant and nominal tip radius values were respectively close to 50 $N.m^{-1}$ and 30 nm. AFM scans of dimensions 6×6 μm^2 were acquired with a resolution close to 47 $nm.px^{-1}$. The PeakForce frequency and amplitude parameters were respectively set to 0.5 kHz and 30 nm for Elium, and 1 kHz and 25 nm for RTM6. In both composite systems, the PeakForce setpoint was selected in order to achieve a 2 to 3 nm indentation depth in the resin. In these conditions, the contact radius remained smaller than 10 nm. The selected PeakForce setpoint values were equal to 150 nN for Elium and 100 nN for RTM6. Modulus images were obtained from the built-in Derjaguin-Muller-Toporov calculation tool of NanoScope 9.4 (Bruker). More information on the acquisition method is presented in [41] for the Elium composite system.

2.6 Finite element modelling

Finite element analyses were carried out using the commercial software Abaqus [42]. The models were created using the exact same geometries as the experimental ROIs. The applied boundary conditions were determined from the displacement profiles measured by DIC on the edges of the respective ROIs. 2D plane stress elements (CPS3) were used for the meshing of the fibres and the matrix to compare with the 2D DIC results. Table 1 presents the material properties used for the mechanical modelling of both composite systems. The carbon or glass fibres were considered as linear elastic. The thermoset matrix was modelled as rate-dependent elasto-plastic using the constitutive continuum model identified and validated by Morelle for RTM6 [43]. In brief, the pressure-dependent yield criterion for the matrix, used to account for the dependence of the polymer to the hydrostatic stress, was defined by a linear Ducker-Prager model, which writes as

$$F = t + p\tan\beta - d = 0, \quad (1)$$

where t is the yield stress, $p = \sigma_{kk}/3$ the pressure (with σ_{kk} the trace of the Cauchy stress tensor), β the friction angle and d the cohesion term. β defines the slope of the yield surface in the p-t plane while t is expressed as

$$t = \frac{\sigma_{eq}}{2}\left[1 + \frac{1}{r} - \left(1 - \frac{1}{r}\right)\left(\frac{I_3}{\sigma_{eq}}\right)^3\right], \quad (2)$$

where σ_{eq} is the von Mises equivalent stress, r the stress ratio between the yield stress under tension and compression and I_3 the third invariant of the deviatoric stress tensor. The associated flow rule writes as $G = \sigma_{eq} + \sigma_{kk}/3 \tan\phi$, with G the flow potential and ϕ the dilation angle. The isotropic hardening law was defined as the sum of three contributions: a pre-peak yield non-linearity, a softening term and a re-hardening capacity (the full description can be found in [43]). The strain rate dependence is considered via the coefficients of the hardening law. Following identification over six decades of strain rate, $r = 1$ and thus $t = \sigma_{eq}$, $\beta = 7.86$ and $\phi = 0$ (assuming plastic incompressibility). A similar model, calibrated for Elium by Maes [44] on four decades of strain rate, was used for the thermoplastic matrix. In that case, $r = 1$ and thus $t = \sigma_{eq}$, $\beta = 26$ and $\phi = 0$. Simulations were performed using Abaqus explicit to overcome convergence issues related to the softening of the matrix, which are difficult to solve with Abaqus Standard (implicit). Perfect interfaces were considered between the fibre and matrix materials, i.e. no damage mechanisms were considered.

3 Results and discussion

3.1 Optimisation and validation of the DIC method

Optimisation of speckle pattern

In addition to providing excellent contrast during imaging, the ideal speckle pattern for a given DIC experiment should meet a number of requirements. The particles should be small with respect to the length scale of the mechanical phenomena of interest, while remaining larger than the image pixel size. Additionally, the distribution of particle sizes should be narrow and speckle density should be high, in order to avoid the presence of 'featureless' subsets in DIC. SEM micrographs of the speckle patterns obtained by e-beam evaporation of indium onto Si wafers for different target coating thicknesses (2, 5, 10, 20 and 50 nm, see section 2.2) are presented in Figure 3, while the associated distributions of particle radii R are displayed as boxplots in Figure 4. Figure 3 shows the increase of the average particle size as more metal gets deposited, though the film remains discontinuous. Moreover, for coating thicknesses larger than or equal to 10 nm, the particles segregate into two distinct populations: the 'large ones' (for which $R \sim 100$ nm), and the 'small ones' (for which $R \sim 10$ nm). Note that the average radius of the larger

particles increases from ~ 50 to ~ 100 and finally ~ 300 nm as target coating thickness is raised from 10 to 20 nm and then 50 nm, respectively. Figure 4 confirms these trends, while providing quantitative information on the evolution of the statistical distribution of particle radii as coating thickness increases. The plots corresponding to the 2 and 5 nm-thick coatings are short and symmetric (see Figure 4 (b)). This indicates a narrow normal distribution for *R* values in both cases, making both coatings potentially eligible for DIC measurements. In this work, only the 5 nm-thick coating was used as a DIC speckle pattern. The 2 nm-thick coating was excluded from the study as the mean particle radius (close to 5 nm) was too close to the smallest pixel size used for SEM imaging (6 $nm.px^{-1}$, see section 2.4). From coating thicknesses of 10 nm onwards, the boxplots get longer and more skewed towards the high *R* values. As described previously, this indicates the emergence of a second, more scattered population of 'large particles' arising from the coalescence of smaller ones. Note that the lower half of the plots (i.e. lower whisker, first quartile and median *R* values) only evolves marginally with coating thickness. This suggests that the size distribution of the 'small particles' remains relatively unchanged. Finally, the selected deposition method developed on Si wafers was applied to a TS composite sample (CFRP) to assess the reproducibility of the speckle pattern on the substrate of interest. Figure 5 shows the corresponding particle size distributions obtained on both materials. The difference in particle size between both substrates remains within the margins of error, consolidating the use of this method on polymer composite specimens.

Choice of DIC input parameters

Table 2 shows the results of the strain deviation analysis described in section 2.4. In all cases, the mean strain value obtained by DIC matches that of the numerically applied strain, with a standard deviation value at least one order of magnitude smaller. Note that this result also confirms the quality of the speckle pattern after optimisation (see section 2.3). The optimum parameters selected for the DIC calculations at both magnification levels were the following: a 10-px subset size (smallest possible size in Ncorr), a 2-px step size and a 5-px strain radius. This combination offers the highest possible spatial resolution for the strain maps, while limiting the amount of noise.

Impact of SEM distortions

As mentioned in the introduction, drift and spatial distortions can cause significant errors in the calculated displacements determined by DIC. Figure 6 is a SEM micrograph showing a ROI that was subjected to a

rigid body motion of -4 µm in the *x*-direction in order to quantify the amplitude of the distortions described in section 2.4. The results of the DIC measurements and corrections are shown in Figure 7. The initial DIC measurements shown in Figure 7 (a) delivered a displacement of around -3.5 µm over the whole ROI. This represents a -0.5 µm discrepancy with respect to the imposed rigid body motion. First, spatial distortions coming from the SEM stage movements were corrected. The corrected displacement field shown in Figure 7 (b) presents an average displacement over the ROI of -3.863 µm. The amplitude of spatial distortions is therefore close to -0.3 µm. Next, the drift distortion field between the initial and displaced states was determined and subtracted from the corrected field of Figure 7 (b). The resulting distortion-free displacement field is shown in Figure 7 (c). The average displacement over the ROI is now -3.9 µm. Comparing Figures 7 (b) and (c) allows quantifying the amplitude of the drift distortion, which is around 0.04 µm. Typically, drift distortions are dominant at high magnification DIC applications. Yet, in the present case, drift distortions are relatively low. This can be related to an excellent grounding of the composite samples via the combination of the conductive carbon coating, evacuating the surface charges, and the silver paste covering the edges of the sample to guide the charges away via the test machine. Thus, proper sample preparation allows overcoming one of the key challenges of nano DIC linked to the excessive amount of drift.

Ultimately, neglecting corrections on DIC measurements for both spatial and drift distortions can induce, at most, an error of around 0.5 µm in the present study. In what follows, the presented DIC maps are systematically corrected for both spatial and drift distortions.

3.2 DIC results

Validation of nano DIC

In order to validate the proposed nano DIC approach, in-situ tests were carried out on the RTM6 and Elium fibre-reinforced systems at a magnification of 20,000. Figures 8 (a) and (c) present the macroscopic load-displacement curves obtained during compression of an RTM6/carbon fibre and an Elium/glass fibre specimen, respectively. In both cases, the alternance of peaks and drops results from specimen relaxation following each load increment (see section 2.4), while the non-linear behaviour at very low displacements is caused by the compression of the soft layer of silver lacquer present on the lateral and lower surfaces of the specimens, i.e. the surfaces in contact with the compression jaws (see section 2.3). Figures 8 (b) and (d) provide a zoomed-out view of the ROIs selected for DIC analysis in

both systems. Note that the ROIs are shown *after* failure, whose loci are indicated with coloured arrows. The force value corresponding to each failure event is shown in Figures 8 (a) and (c). For the RTM6 specimen, failure occurs within the ROI via interface debonding, see Figure 8 (b). For the Elium/glass fibre specimen, however, two subsequent failure events are reported. First, a crack opens in the matrix outside the ROI but close to its boundaries (green arrow), and interface debonding then occurs within the ROI (red arrow), see Figure 8 (d). In this section, only the displacement and strain fields recorded just before each failure event are presented. The corresponding DIC strain maps are presented in Figures 9 and 10, respectively.

Figures 9 (a) and (b) show the ε_{xx} and ε_{xy} strain fields for the RTM6 system. Nano DIC clearly distinguishes the fibre and matrix response. Indeed, being much stiffer than the matrix, the average amplitudes of ε_{xx} and ε_{xy} are close to zero in the fibres. The fibre/matrix interface can also easily be distinguished, which suggests that the resolution of nano DIC is sufficient to avoid smoothing of the fibre and matrix strains. The ε_{xx} and ε_{xy} strain fields displayed in Figures 10 (a), (c) and (b), (d), respectively, show the analogous results for the Elium system. Hence, the combination of a high-quality nanoscale speckle pattern and careful specimen preparation (i.e. grounding, etc.) allows overcoming the main restriction related to the use of micro DIC on FRPs in the literature. The proper phase separation in the DIC results opens the door to investigate the interphase behaviour of FRPs. To illustrate this, Figures 9 (c) and (d), as well as Figures 10 (e) and (f) show the strain distribution along different paths (depicted as white dashed lines) for both systems. A transition zone between the fibre and the matrix is systematically present. Within this region, a smooth transition from the quasi-zero strain level of the fibres to the matrix strains is observed. This transition zone spreads over 200 nm to 500 nm (assuming a peak-to-peak width). The literature reports that an interphase layer exists in FRPs that can spread from a few hundreds of nanometres to a few microns depending on the fibre sizing and curing conditions [14,16,45]. Hence, the observed transition zone can be related to the interphase of each system.

Localised areas of large strain amplitudes in between fibres are captured by DIC, as observed in Figures 9 (b) and 10 (b) for the RTM6 and Elium systems, respectively. Note that high strain amplitudes are systematically found around fibres, highlighting the importance of getting accurate DIC measurements in both fibre and matrix zones. In particular, shear strain localisation is visible at the bottom right of Figure 9 (b) for RTM6 and near the right fibre-matrix interface in Figure 10 (d) for Elium. Comparing these two regions with the loci of interface debonding depicted in Figures 8 (b) and (d) for

RTM6 and Elium, respectively, large shear strains accumulate exactly where failure ensues. In the case of Elium, DIC also captures the redistribution of strains following a matrix cracking event starting outside the ROI, indicated in Figures 8 (c) and (d) by the green arrows. This is especially clear when comparing Figures 10 (a) and (c), which show the ε_{xx} strain fields before and after the event. One can notice the homogenisation of the matrix strain field in Figure 10 (c), with respect to Figure 10 (a). The same trend is also observed, to a lesser extent, when comparing Figures 10 (b) and (d) in terms of the shear strains ε_{xy}. Figure 21 in the annex displays the maximum shear strain maps for RTM6 and Elium, which clearly indicate that the maxima of shear coincide with the loci of failure in both systems.

Surprisingly, shear bands propagating between two fibres are not observed in any of the two systems, contrary to what is expected in FRPs subjected to transverse compression [3]. Still, in Figure 9 (b), strain concentrations can be found not only near the bottom of the right-hand fibre (i.e. in the region where a crack follows), but also near the top of the left-hand fibre. This could suggest that a shear band started to develop in the RTM6 ROI, but could not propagate as the induced localisation led the fibre/matrix interface failure first. Hence, the lack of significant shear banding measured by DIC may simply be related to an unfortunate choice of region of interest for a given test. Or, as the observed ROIs are quite small in both systems, it is also possible that large-scale shear band formations are missed. Therefore, further investigation will require a screening of more regions of interest per specimen during each compression test, in order to identify and quantify the presence and amplitudes of micro shear bands.

In addition to the DIC measurements presented above, post-mortem SEM observations were carried out outside the ROIs to analyse the failure behaviour of both systems. The fracture surfaces are presented in Figure 11 for RTM6 and Figure 12 for Elium, for different length scales. The micrographs in Figures 11 (a) and (b) suggest that failure initiates suddenly in the RTM6 composite. The crack path follows the fibre/matrix interface, though no sign of progressive damage from interface decohesion or matrix cracking was observed, as demonstrated in Figures 11 (c) and (d). Still, Figure 11 (c) shows that the conductive coating displays a significant amount of micro cracks, confirming that the RTM6 matrix below undergoes strong local plastic deformation via the creation of nano or micro shear bands. These observations are in line with the results of Chevalier et al. [3]. Lastly, a close-up of the fibre/matrix interface in Figure 11 (d) shows the absence of crazes, which reinforces the idea of the absence of damage at the interfaces. The case of the Elium system in Figures 12 (a) and (b) is different, showing clear signs of damage accumulation all over the matrix. Note that this difference in behaviour between the two

composite systems can also be inferred from the load-displacement curves presented in Figures 8 (a) and (c), which respectively suggest that the RTM6 macroscopically fails in a brittle manner, whereas the Elium system only fails after entering global plasticity. However, these differences as well as those observed on the post-mortem SEM micrographs may partially be explained by the difference in specimen geometry, which leads to different levels of stress triaxiality associated to the barrelling effect. Still, Figure 12 (c) clearly indicates strong plastic deformation in the Elium matrix via micro shear bands developing in between fibres. Finally, in Figure 12 (d) crazes of around 20 nm in thickness can be observed, confirming that progressive damage accumulates within the Elium matrix during deformation. Ultimately, the DIC analysis is thus able to identify the regions of stress concentration near the fibre/matrix interface that lead to failure for systems that involve progressive damage, such as the Elium/glass fibre composite, and for those that do not, like the RTM6/carbon fibre composite.

Although the above analysis demonstrates the potential of the nano DIC approach, DIC artefacts are still detected in Figures 9 and 10. The potential sources for these artefacts are presented in Figure 13, using SEM micrographs of both ROIs before and after failure. In particular, a clustering of indium particles indicated by arrow 1 in Figure 13 (a) results in an unclear separation between the fibre and matrix strains in RTM6, see Figures 9 (a) and (b). This particle clustering is most likely due to differential erosion between the fibre and the matrix that was created during the polishing phase (< 50 nm difference). The presence of shallow leftover polishing scratches on the matrix is made more visible by the indium deposition, as shown by arrow 2. This leads to spurious strain fluctuations in the DIC maps of RTM6, which are most visible in Figure 9 (a). Finally, the combination of deformation around the fibres and repeated observation can lead to some charging of the interfaces, as shown by arrows 3 and 4 where the fibre/matrix interface is whitened. The charging effect decreases the contrast within these whitened zones, potentially leading to a loss of correlation in some cases. Hence, although the novel nano DIC approach allows reaching high resolution and achieving proper DIC characterisation of heterogeneous material systems such as FRPs, careful specimen preparation is crucial to avoid any artefacts.

Investigating the interphase behaviour

The previous section showed that a transition region of a few hundreds of nanometres exists in the strain fields between the fibres and the matrix. It presumably corresponds to the fibre/matrix interphase. To confirm that nano DIC is a viable and relatively direct alternative to measure the interphase size of FRPs, DIC was performed on successive images during a single test. At each load, the current image was

compared to the reference image, to avoid propagation of artefacts. The aim was to study whether the transition zone size changes during the test, which would indicate that it does not correspond to the interphase. Figure 14 shows the ε_{xx} field at different moments during the test for RTM6. Figure 15 presents the same for Elium. For each system, the strains were evaluated along paths crossing at least two fibre/matrix interfaces. The results are given in Figure 16. In both systems, for all three paths, the amplitude of the maximum strain attained in the transition zone increases during the test. The thickness of the zones grows marginally up until the last load before failure.

For RTM6, path 1 crosses through very thin matrix regions in between fibres whereas path 2 traverses a single large matrix pocket. Yet, the transition zone thickness in paths 1 and 2 is around 300-400 nm. This is in line with the aforementioned results of Figure 9. Considering the thin matrix ligaments in path 1, it is questionable whether defining a distinct interphase is meaningful as the ligament size is roughly 300 nm as well. If the matrix is capable of developing an interphase in such a confined space, then it would imply that in such regions, the mechanical response is entirely dictated by the interphase layer properties (which differ from the bulk matrix). As failure systematically occurs by sudden debonding of the fibre/matrix interface, these findings highlight the importance of studying the interphase surrounding the fibres. For Elium, the transition zone along path 3 is about 400 nm as well. Again, this result correlates well with the results of Figure 10.

To confirm the DIC results, AFM measurements were performed on both composite systems. The AFM modulus map of Figure 17 (a) shows two profiles along a path from the carbon fibre to the RTM6 matrix. The evolution of the modulus along these profiles is given in Figure 17 (b). An interphase layer of around 150 nm can be identified for this system. Similarly for Elium, the profiles shown in Figures 17 (c) and (d) indicate the presence of a 200-nm interphase region between the glass fibre and the Elium matrix. For both systems, the interphase thickness measured by AFM is on the same order of magnitude as the width of the transition zone captured by DIC, i.e. a few hundreds of nanometres. Note that the interphase thickness varies within a given system, depending on (1) the amount of sizing present on each fibre, (2) the local fibre arrangement, and also on (3) the matrix pocket size [13-16]. This reinforces the idea that nano DIC is capable of capturing interphases in FRPs relatively well.

Ultimately, nano DIC appears as a promising tool to detect the interphase of FRPs. As this technique is simpler to set up than AFM (less tedious sample preparation), it offers a convenient alternative. Furthermore, it provides quantitative data about the deformability while AFM remains semi-quantitative

regarding the magnitude of the local stiffness. Now, extracting material properties from DIC requires inverse identification through modelling.

3.3 Comparison to FE simulations

In an attempt to evaluate the validity of using calibrated continuum models for micro-mechanical analyses, FE simulations were carried out on the ROIs presented in Figures 8 (b) and 8 (d) for the RTM6 and Elium FRPs, respectively. The ε_{xx} and ε_{xy} fields measured by DIC and predicted by FEA are compared in Figures 18 (RTM6) and 19 (Elium). For RTM6, the predicted strain distribution and amplitude within the large matrix pocket fit well with the DIC measurements, in particular for ε_{xx}, see Figures 18 (a) and (b). However, in the thin matrix bands at the top, the model drastically overestimates the strains compared to DIC. Within the ε_{xy} map, the opposing diagonal shear pattern around the fibres is also captured by FEA, as shown in Figures 18 (d) and (e). Yet, the strain amplitude of the shear accumulation around the fibres is, again, largely overestimated. This is further illustrated in Figures 18 (c) and (f) along a path. Furthermore, no transition zone at the interface is predicted by the model. The comparison between FE and DIC analyses for Elium before the 2nd failure event, which is displayed in Figure 19, yields the same conclusions. In Figures 19 (b) and (e), the average ε_{xx} and ε_{xy} strain distributions within the matrix fit well with the DIC results in Figures 19 (a) and (d), yet some discrepancies remain as, for example, the presence of a positive shear strain around the left-hand fibre in Figure 19 (e) compared to Figure 10 (d). Figures 19 (c) and (f) show the strain variations along a path for both DIC and FEA. At the interfaces, a sharp transition with higher strain amplitudes is once more seen, indicating that no interphase is predicted by FEA for both systems. Furthermore, in Figure 19 (e), the size of the positive strain band in the bottom right extends further, leading to an inversion to positive rather than negative strains along the path.

The validity of the use of the continuum of Morelle et al. [43] was already questioned by Chevalier et al [3]. He demonstrated that the model overestimates the strain amplitudes in matrix pockets, while the overall strain distribution remains close to DIC measurements. The present FE results are therefore not surprising. However, the comparison between FEA and DIC clearly shows that the interphase region around the fibres is crucial. As the presence of the interphase can be confidently confirmed by DIC, assuming a homogeneous matrix within the FE framework limits its ability to accurately model the load

transfer at the interfaces. In addition, neglecting the presence of progressive damage is a reasonable assumption for RTM6 (and may be debated for Elium). This suggests that micro-mechanical modelling strategies should consider the presence of an interphase with intrinsic stiffness and hardness larger than the bulk matrix, as indicated by the AFM maps for the Young's modulus. Chevalier et al. pointed out two possibilities to overcome the discrepancy between the DIC and FEA. The first is related to intrinsically different local properties in the matrix, which may arise from difference in curing conditions due to the presence of near fibres. The present study indeed suggests local variations in the properties of the matrix due the presence of an interphase around the fibres. The second possibility assumes true size-dependent plasticity [46–49]. This last aspect requires further investigations to determine if this second effect plays an important role, in the addition to the interphase effect.

4 Conclusion

The development of predictive micromechanics-based multiscale models requires accurate data about the local fibre/matrix level deformation and failure, as well as a deep understanding of the mechanisms themselves in order to select the right ingredients in the constitutive model. In this study, the use of DIC on FRPs was extended to the nanoscale to determine the deformation behaviour of the matrix in the vicinity of fibres. To this end, a novel nanoscale speckle pattern deposition technique was simplified and used on UD fibre-reinforced thermoplastic and thermoset polymers. In order to assess the robustness of the experimental approach, the quality of the speckle pattern was carefully checked and SEM-induced distortions were quantified. The main challenges associated to the use of nanoscale DIC on FRPs are linked to charging effects in the SEM and related drift distortions. This assessment ensures that the proposed DIC analysis is quantitative. A comparison with FE predictions was performed to determine the differences with DIC. The main findings of this study are the following:

- Careful specimen preparation of FRPs allows minimising spatial and drift distortion-related errors.
- The nano DIC approach accurately determines displacement and strain fields at the local fibre/matrix scale, despite the significant contrast in mechanical properties between the constituents. Hence, the main issue reported in the literature of submicron level DIC was overcome.
- The local micro shear band formation and interface failure are well captured in the DIC maps within highly confined material regions, even though the strain gradients are very steep.

- DIC data reveal the systematic presence of an interphase around the fibres for both material systems. The measured interphase width perfectly relates to the AFM measurements made on the same material system.
- The average strain amplitude predicted by FEA in large matrix pockets agrees with DIC. However, the strain distribution and localisation differ, especially in the near fibre region. In particular, the FEA largely overestimates the strain concentration within confined regions and/or at the fibre/matrix interface.

In the end, this study provides a robust method to acquire data about the mechanics of FRPs at submicron levels. The interphase of FRPs can be easily and reliably measured in comparison to other techniques. The importance of characterising the matrix at this scale is highlighted by the inability of FEA using continuum models to reproduce the experimental results in conditions where the matrix is the main carrier of the deformation. As failure occurs at the fibre/matrix interface, it may be necessary to include an interphase region around the fibres and maybe strain gradient plasticity effects to accurately model the load transfer occurring between the matrix and fibre. Still, this means that quantitative data in the interphase region need to be gathered. The physical reason behind the difference in response of the interphase remains unknown. It may be due to different local curing conditions and strain gradient effects.

Acknowledgments

The UCLouvain team deeply acknowledges fruitful discussion and guidance from J. Hoefnagels and T. Vermeij from TU Eindhoven, and Y. Swolfs and C. Breite from KULeuven. NK is a research fellow of the Fonds de la Recherche Scientifique de Belgique - FNRS and gratefully acknowledges their support. SG and TP gratefully acknowledge the financial support from Arkema. Computational resources have been provided by the supercomputing facilities of the Université catholique de Louvain (CISM/UCL) and the Consortium des Équipements de Calcul Intensif en Fédération Wallonie Bruxelles (CÉCI) funded by the Fonds de la Recherche Scientifique de Belgique (F.R.S-FNRS).

Appendix

The distortion correction analysis presented in section 2.4 stated that the impact of the displacement distortion correction on the strain fields was negligible. Figure 20 presents the strain maps obtained after each correction. The strain variations are one order of magnitude below the measured strain amplitudes in

the main DIC analysis. Figure 21 presents the maximum shear strain maps discussed briefly in section 3.2. The maps clearly show that failure coincides with the areas of strain concentration.

References

[1] LLorca J, González C, Molina-Aldareguía JM, Lópes CS. Multiscale Modeling of Composites: Toward Virtual Testing … and Beyond. JOM 2013;65:215–25.

[2] Melro A, Camanho PP, Pires FA, Pinho S. Micromechanical analysis of polymer composites reinforced by unidirectional fibres: Part ll – micromechanical analyses. Int J Solids Struct 2013;50:1906–15.

[3] Chevalier J, Camanho PP, Lani F, Pardoen T. Multi-scale characterization and modelling of the transverse compression response of unidirectional carbon fiber reinforced epoxy. Compos Struct 2019;209:160–76.

[4] Pardoen T, Klavzer N, Gayot S, Van Loock F, Chevalier J, Morelle X, et al. Nanomechanics serving polymer-based composite research. Comptes Rendus Phys 2021;22:1–22.

[5] Hardiman M, Vaughan TJ, McCarthy CT. A review of key developments and pertinent issues in nanoindentationtesting of fibre reinforced plastic microstructures. Compos Struct 2017;180:782–98.

[6] Han C. Indentation Size Effect in Polymers. Adv Mater Sci Res 2011;10:393–413.

[7] Voyiadjis GZ, Malekmotiei L. Variation of the Strain Rate During CSM Nanoindentation of Glassy Polymers and Its Implication on Indentation Size Effect. J Polym Sci, Part B Polym Phys 2016;54:2179–87.

[8] Naya F, González C, Lopes CS, Llorca J. Combined multi-scale simulations in fiber-reinforced composites. Proc. 20th International Conference on Composite Materials (ICCM20), Copenhagen, Denmark: 2015, 22-6.

[9] Tan W, Naya F, Yang L, Chang T, Falzon BG, Zhan L, et al. The role of interfacial properties on the intralaminar and interlaminar damage behaviour of unidirectional composite laminates: Experimental characterization and multiscale modelling. Compos Part B Eng 2018;138:206–21.

[10] Nikaeen P, Samadi-Dooki A, Voyiadjis GZ, Zhang P, Chirdon WM, Khattab A. Effect of plastic deformation on the nanomechanical properties of glassy polymers: An experimental study. Mech Mater 2021;159:103900.

[11] Alisafaei F, Han C-S. Indentation Depth Dependent Mechanical Behavior in Polymers. Adv Condens Matter Phys 2015:1–20.

[12] Rodríguez M, Molina-Aldareguía JM, González C, Llorca J. Determination of the mechanical properties of amorphous materials through instrumented nanoindentation. Acta Mater 2012;60:3953–64.

[13] Bogetti TA, Wang T, VanLandingham MR, Gillespie JW. Characterization of nanoscale property variations in polymer composite systems: 2. Numerical modeling. Compos Part A Appl Sci Manuf 1999;30A:85–94.

[14] Munz M, Sturm H, Schulz E, Hinrichsen G. The scanning force microscope as a tool for the detection of local mechanical properties within the interphase of fibre reinforced polymers. Compos Part A Appl Sci Manuf 1998;29:1251–9.

[15] Winter RM, Houston JE. Interphase mechanical properties in an epoxy-glass fiber composite as measured by interfacial microscopy. Proc. SEM Spring Conference Experimental Applied Mechanics Experimental/Numerical Mechanics Electronic Packaging III, Houston, Texas (USA): 1998, p. 355–8.

[16] Downing TD, Kumar R, Cross WM, Kjerengtroen L, Kellar JJ. Determining the interphase thickness and properties in polymer matrix composites using phase imaging atomic force microscopy and nanoindentation. J Adhes Sci Technol 2000;14:1801–12.

[17] Canal LP, González C, Molina-Aldareguía JM, Segurado J, LLorca J. Application of digital image correlation at the microscale in fiber-reinforced composites. Compos Part A Appl Sci Manuf 2012;43:1630–8.

[18] Mehdikhani M, Aravand M, Sabuncuoglu B, Callens MG, Lomov S V, Gorbatikh L. Full-field strain measurements at the micro-scale in fiber-reinforced composites using digital image correlation. Compos Struct 2016;140:192–201.

[19] Bornert M, Brémand F, Doumalin P, Dupré J-C, Fazzini M, Grédiac M, et al. Assessment of Digital Image Correlation Measurement Errors: Methodology and Results. Exp Mech 2009;49:353–70.

[20] Lagattu F, Bridier F, Villechaise P, Brillaud J. In-plane strain measurements on a microscopic

scale by coupling digital image correlation and an in situ SEM technique. Mater Charact 2006;56:10–8.
[21] Totry E, González C, LLorca J, Molina-Aldareguía JM. Mechanisms of shear deformation in fiber-reinforced polymers: experiments and simulations. Int J Fract 2009;158:197–209.
[22] Catalanotti G, Camanho PP, Xavier J, Dávila CG, Marques AT. Measurement of resistance curves in the longitudinal failure of composites using digital image correlation. Compos Sci Technol 2010;70:1986–93.
[23] Lomov S V, Ivanov DS, Verpoest I, Zako M, Kurashiki T, Nakai H, et al. Full-field strain measurements for validation of meso-FE analysis of textile composites. Compos Part A Appl Sci Manuf 2008;39:1218–31.
[24] Mehdikhani M, Matveeva A, Aravand MA, Wardle BL, Lomov S V, Gorbatikh L. Strain mapping at the micro-scale in hierarchical polymer composites with aligned carbon nanotube grafted fibers. Compos Sci Technol 2016;137:24–34.
[25] Carter JLW, Uchic MD, Mills MJ. Impact of Speckle Pattern Parameters on DIC Strain Resolution Calculated from In-situ SEM Experiments. In: Carroll J, Daly S, editors. Fract. Fatigue, Failure, Damage Evolution, Volume 5, Cham, Switzerland: Springer International Publishing; 2015, p. 119–26.
[26] Montgomery CB, Koohbor B, Sottos NR. A robust patterning technique for electron microscopy-based digital image correlation at sub-micron resolutions. Exp Mech 2019;59:1063–73.
[27] Lagattu F, Bridier F, Villechaise P, Brillaud J. In-plane strain measurements on a microscopic scale by coupling digital image correlation and an in situ SEM technique. Mater Charact 2006;56:10–8.
[28] Hoefnagels JPM, van Maris MPFHL, Vermeij T. One-step deposition of nano-to-micron-scalable, high-quality digital image correlation patterns for high-strain in-situ multi-microscopy testing. Strain 2019;55:12330.
[29] Jung YS, Lee DW, Jeon DY. Influence of dc magnetron sputtering parameters on surface morphology of indium tin oxide thin films. Appl Surf Sci 2004;221:136–42.
[30] Sutton MA, Li N, Joy DC, Reynolds AP, Li X. Scanning electron microscopy for quantitative small and large deformation measurements part I: SEM imaging at magnifications from 200 to 10,000. Exp Mech 2007;47:775–87.
[31] Sutton MA, Li N, Garcia D, Cornille N, Orteu JJ, McNeill SR, et al. Scanning Electron Microscopy for Quantitative Small and Large Deformation Measurements Part II: Experimental Validation for Magnifications from 200 to 10,000. Exp Mech 2007;47:789–804.
[32] Maraghechi S, Hoefnagels JPM, Peerlings RHJ, Rokoš O, Geers MGD. Correction of Scanning Electron Microscope Imaging Artifacts in a Novel Digital Image Correlation Framework. Exp Mech 2019;59:489–516.
[33] Maraghechi S, Hoefnagels JPM, Peerlings RHJ, Geers MGD. Correction of scan line shift artifacts in scanning electron microscopy: An extended digital image correlation framework. Ultramicroscopy 2018;187:144–63.
[34] Mello AW, Book TA, Nicolas A, Otto SE, Gilpin CJ, Sangid MD. Distortion Correction Protocol for Digital Image Correlation after Scanning Electron Microscopy: Emphasis on Long Duration and Ex-Situ Experiments. Exp Mech 2017;57:1395–409.
[35] Kammers AD, Daly S. Digital image correlation under scanning electron microscopy: methodology and validation. Exp Mech 2013;53:1743–61.
[36] Vacuum Engineering & Materials. VEM Thin Film Evaporation Guide 2017.
[37] High Purity Evaporation Materials - Heeger Materials Inc n.d.
[38] CDC - NIOSH Pocket Guide to Chemical Hazards - Indium n.d.
[39] Blaber J, Adair B, Antoniou A. Ncorr: Open-Source 2D Digital Image Correlation Matlab Software. Exp Mech 2015;55:1105–22.
[40] Minne SC, Hu Y, Hu S, Pittenger B, Su C. Nanoscale quantitative mechanical property mapping using peak force tapping atomic force microscopy. Microsc Microanal 2010;16:464–5.
[41] Gayot SF, Klavzer N, Bailly C, Pardoen T, Gérard P, Nysten B. Micromechanical characterization of local polymer properties in fibre-reinforced composite vs. neat polymer. Under Submiss 2022.
[42] ABAQUS Inc. ABAQUS/Explicit. ABAQUS Doc 2005:1–28.
[43] Morelle XP, Chevalier J, Bailly C, Pardoen T, Lani F. Mechanical characterization and modeling of the deformation and failure of the highly crosslinked RTM6 epoxy resin. Mech Time-Dependent Mater 2017;21:419–54.
[44] Maes M. Mechanical properties of high performance recyclable thermoplastic based composites. Master Thesis, Univ Cathol Louvain 2020.

[45] Vanlandingham MR, McKnight SH, Palmese GR, Bogetti TA, Eduljee RF, Gillespie JW. Characterization of interphase regions using atomic force microscopy. MRS Proc 1996;458:313.
[46] Chong ACM, Lam DCC. Strain gradient plasticity effect in indentation hardness of polymers. J Mater Res 1999;14:4103–10.
[47] Chandrashekar G, Han C-S. Length scale effects in epoxy: The dependence of elastic moduli measurements on spherical indenter tip radius. Polym Test 2016;53:227–33.
[48] Alisafaei F, Han C-S, Lakhera N. Characterization of indentation size effects in epoxy. Polym Test 2014;40:70–8.
[49] Jebahi M, Forest S. Scalar-based strain gradient plasticity theory to model size-dependent kinelatic hardening effects. Continuum Mech. Thermodyn. 2021; 33:1223–1245.

Table 1:

	E_{11} (GPa)	E_{22} (GPa)	E_{33} (GPa)	ν_{12}	ν_{23}	ν_{31}	Density (g.cm^{-3})
Carbon fibres	238	28	28	0.28	0.33	0.02	1.8
Glass fibres	80	-	-	0.22			2.54
RTM6 matrix	3	-	-	0.34	-	-	1.14
Elium resin	2.8	-	-	0.35	-	-	1.17

Table 2:

Magnification level	Subset size (px)	Step size (px)	Strain radius (px)	Mean strain (-)	Strain standard deviation (-)
10,000	30	2	5	0.0101	5.07E-05
10,000	20	2	5	0.0101	8.33E-05
10,000	10	2	5	0.0101	2.10E-04
10,000	10	2	3	0.0101	3.59E-04
10,000	10	2	1	0.0101	7.99E-04
10,000	10	1	5	0.0101	3.20E-04
10,000	20	1	5	0.0101	1.09E-04
10,000	10	1	3	0.0101	4.90E-04
10,000	10	1	1	0.0101	1.10E-03
20,000	30	2	5	0.0121	4.65E-05
20,000	20	2	5	0.0121	7.47E-05
20,000	10	2	5	0.0121	1.50E-04
20,000	10	2	3	0.0121	2.37E-04
20,000	10	2	1	0.0121	5.40E-04
20,000	10	1	5	0.0121	2.32E-04
20,000	20	1	5	0.0121	9.45E-05
20,000	10	1	3	0.0121	3.38E-04
20,000	10	1	1	0.0121	7.79E-04

Figure 1: Unidirectional composite specimens for in-situ transverse compression testing: (a) glass fibre-reinforced TP and (b) carbon fibre-reinforced TS. Fibre orientation is parallel to the *z*-axis and compression is performed in the *x*-direction. All dimensions are in mm.

Figure 2: Thermoplastic composite specimen mounted on microtest compression stage.

Figure 3: Optimisation of the speckle pattern for DIC measurements: SEM images of a (a) 2 nm, (b) 5 nm, (c) 10 nm, (d) 20 nm and (e) 50 nm-thick indium speckle deposited by e-beam evaporation onto Si wafers.

Figure 4: Particle size distribution of indium speckle patterns with target thicknesses of (a) 2 to 50 nm and (b) 2 and 5 nm.

Figure 5: Comparison of particle size distributions obtained for a 5 nm-thick indium speckle pattern deposited onto two different substrates: Si wafer vs. carbon fibre-reinforced TS composite.

Figure 6: Region of interest for the quantification of the spatial and drift distortion amplitudes.

Figure 7: Horizontal displacement field measured by DIC: (a) without any correction, (b) after spatial correction and (c) after spatial and drift corrections.

Figure 8: Macroscopic load-displacement curves obtained from the in-situ compression testing and SEM micrographs of the corresponding ROIs used for DIC analysis of: (a) and (b) an RTM6/carbon fibre specimen and (c) and (d) an Elium/glass fibre specimen. Coloured arrows indicate the location of failure events observed within or close to the ROIs during testing, and the same colour code is used to show force-displacement values at these moments.

Figure 9: Strain maps and evolution of strain profiles across the carbon fibre-RTM6 matrix interface (white dashed line) obtained by DIC: (a) along the *x* and (b) x*y* directions.

Figure 10: Strain maps obtained by DIC in the Elium/glass fibre specimen along the *x* direction, (a) before 1st failure event and (c) before 2nd failure event, and along the *xy* directions (b) before 1st failure event and (d) before 2nd failure event, alongside with corresponding strain profiles across the fibre-matrix interface (white dashed line) in the (e) *x* and (f) *xy* directions. The terms '1st and 2nd cracks' refer to the failure events identified in Figure 8.

Figure 11: RTM6 – Post-mortem observations of the failed material surface: (a) general overview, (b) main crack, (c) fibre/matrix level interface failure, (d) zoom of the interface failure in (c).

Figure 12: Elium – Post-mortem observations of the failed material surface: (a) general overview, (b) main cracks, (c) fibre/matrix level diffuse cracks and shear bands, (d) zoom of the cracks in (c).

Figure 13: Comparison between initial and final (post-failure) images for two ROIs: RTM6 system (a) in initial state versus (b) after failure, and Elium system (c) in initial state versus (d) after failure. Note that the failure regions are highlighted by white ellipses, while the white arrows represent source of imperfection for the DIC analysis.

Figure 14: RTM6 - Horizontal ε_{xx} strain map at four different stages during the in-situ compression test until the last moment before failure: (a) at 600 N, (b) at 850 N, (c) at 1000 N and (d) at 1150 N.

Figure 15: Elium - Horizontal ε_{xx} strain map at four different stages during the in-situ compression test until the last moment before failure: (a) at 500 N, (b) at 700 N, (c) at 1000 N and (d) at 1300 N.

Figure 16: Evolution of the horizontal ε_{xx} strain along the three numbered profiles shown in Figures 14 and 15 at different stages during the in-situ compression test: (a) and (b) profiles 1 and 2 on RTM6, respectively; (c) profile 3 on Elium. An interphase of around 300 nm marked by the shaded area is visible for both systems.

Figure 17: Atomic force microscopy measurements obtained by PeakForce Tapping® on (a), (b) the RTM6/carbon fibre composite, and (c), (d) the Elium/glass fibre composite. DMT modulus maps are presented on Figures (a) and (c), while (b) and (d) show the evolution of the DMT modulus along two profiles extracted from each map.

Figure 18: RTM6 – Horizontal ε_{xx} strain field (a) measured by DIC versus (b) predicted by FEA using a continuum model, and (c) comparison of strain evolution along the white dashed profile for both DIC and FEA. (d), (e) and (f) show the equivalent in terms of shear strains ε_{xy}.

Figure 19: Elium, before 2nd failure event – Horizontal ε_{xx} strain field (a) measured by DIC versus (b) predicted by FEA using a continuum model, and (c) comparison of strain evolution along the white dashed profile for both DIC and FEA. (d), (e) and (f) show the equivalent in terms of shear strains ε_{xy}.

Figure 20: Horizontal ε_{xx} strain field measured by DIC: (a) without any correction, (b) after spatial correction and (c) after spatial and drift correction.

Figure 21: Maximum shear γ_{max} strain fields obtained by DIC (a) in the RTM6/carbon fibre system and (b), (c) in the Elium/glass fibre system before 1st failure event and before 2nd failure event, respectively.

Table 1: Elastic properties of the fibre and matrix materials used for the FE modelling of the TP and TS composite systems.

Table 2: Strain deviation analysis [33] results obtained for various sets of DIC parameters.

Credit Author Statement

Nathan Klavzer: Conceptualization, Methodology, Software, Validation, Formal analysis, Investigation, Writing - Original Draft, Writing - Review & Editing, Visualization. **Sarah Gayot:** Conceptualization, Methodology, Validation, Formal analysis, Investigation, Writing - Original Draft, Writing - Review & Editing, Visualization. **Michaël Coulombier:** Conceptualization, Methodology, Writing - Original Draft, Writing - Review & Editing. **Bernard Nysten**: Conceptualization, Resources, Writing - Review & Editing, Supervision. **Thomas Pardoen**: Conceptualization, Resources, Writing - Review & Editing, Supervision, Funding acquisition.

conflict of Interest Statement

Declaration of interests

☒The authors declare that they have no known competing financial interests or personal relationships that could have appeared to influence the work reported in this paper.

☐The authors declare the following financial interests/personal relationships which may be considered as potential competing interests:

Figure 1

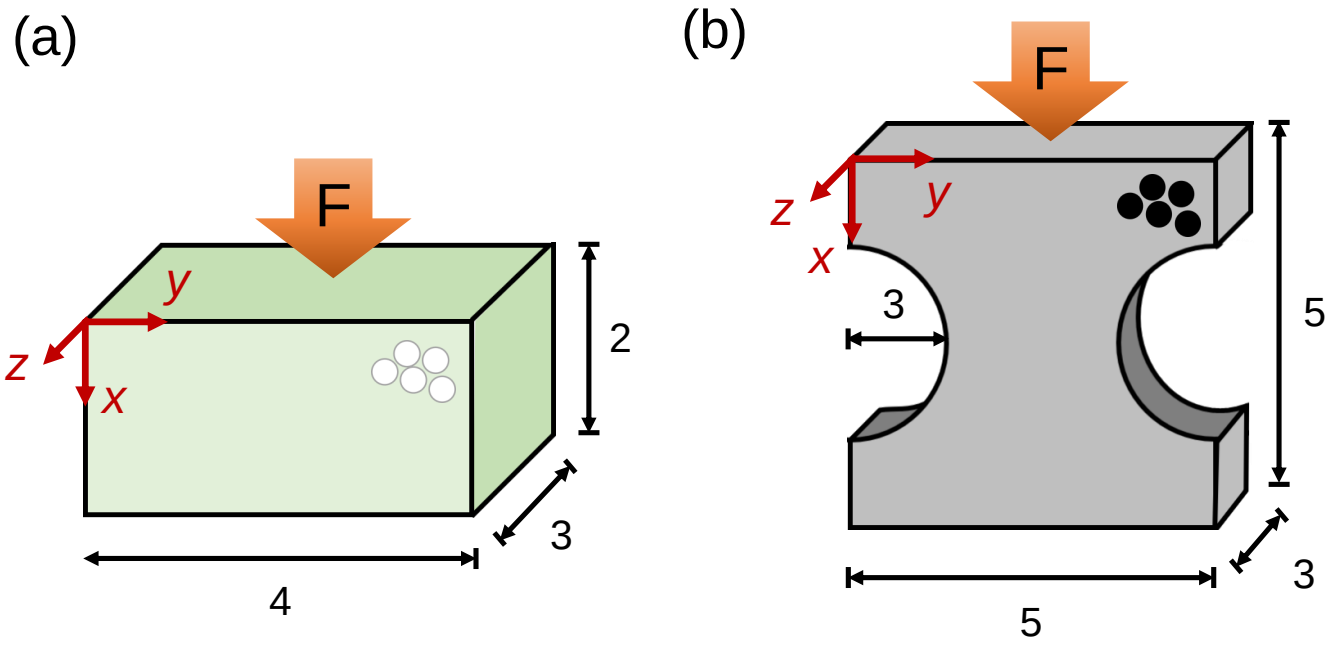

Figure 2

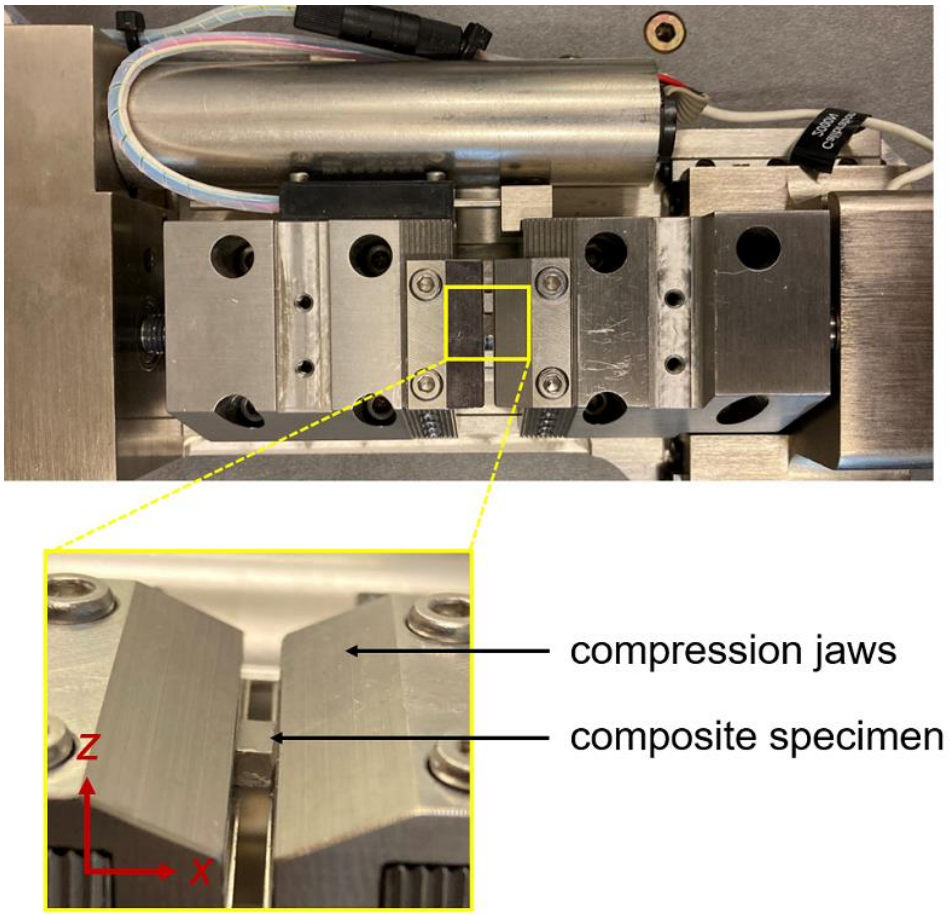

Figure 3

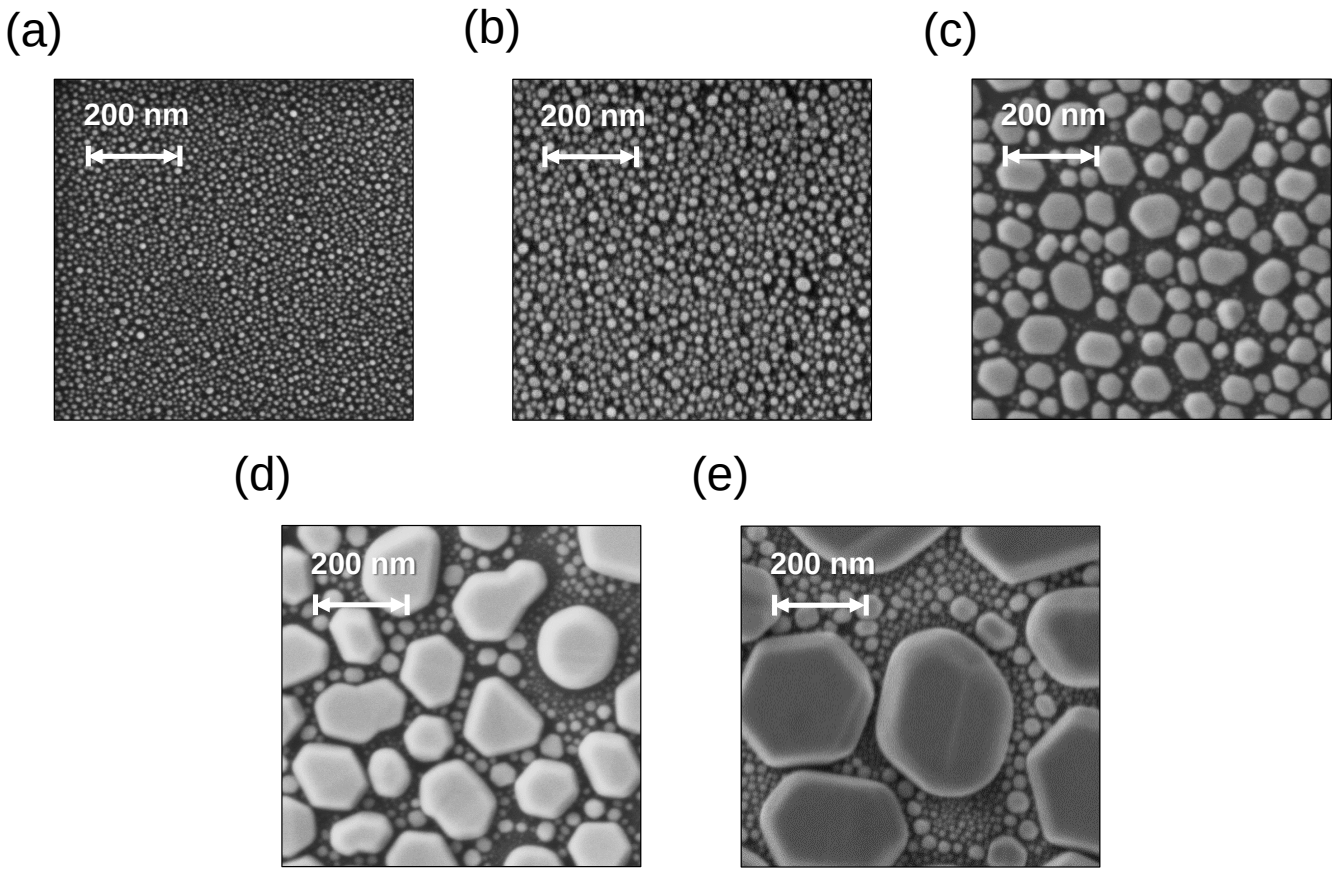

Figure 4

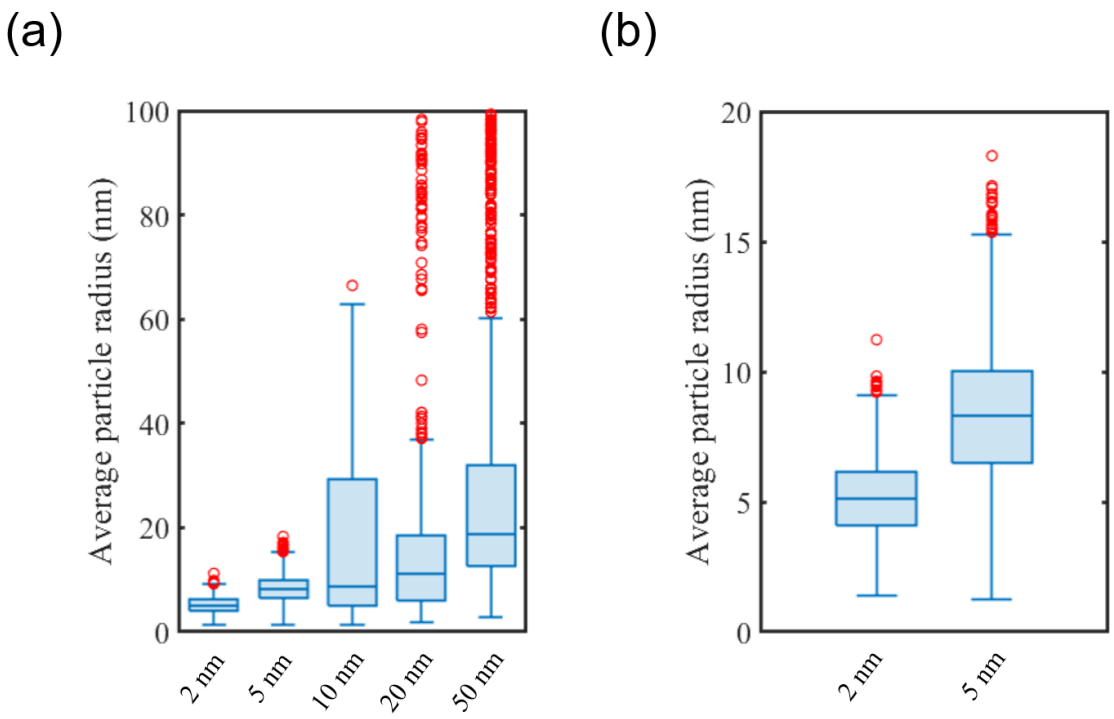
(a)
(b)
Average particle radius (nm)
100
80
60
40
20
0
2 nm
5 nm
10 nm
20 nm
50 nm
Average particle radius (nm)
20
15
10
5
0
2 nm
5 nm

Figure 5

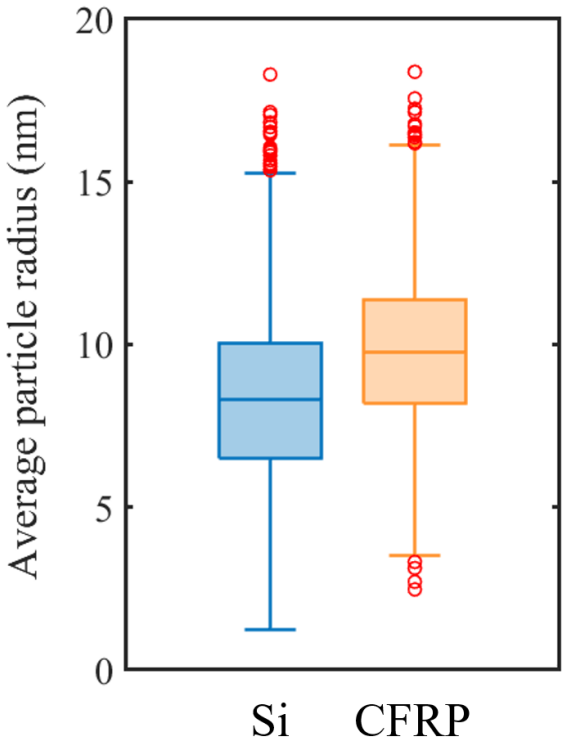

Figure 6

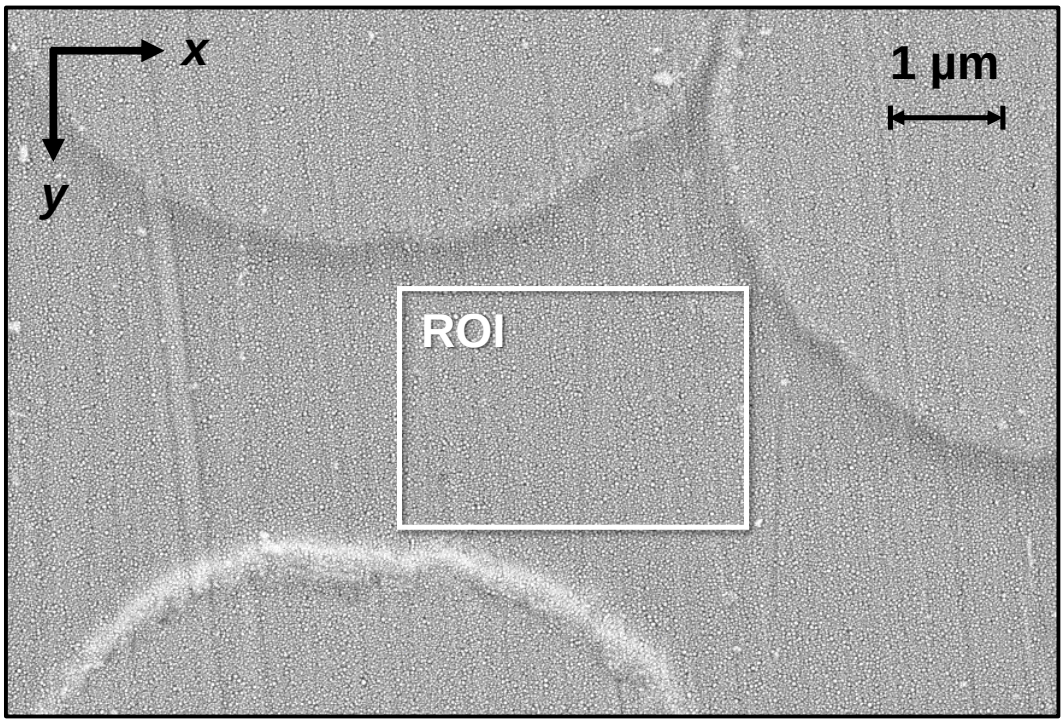

Figure 7

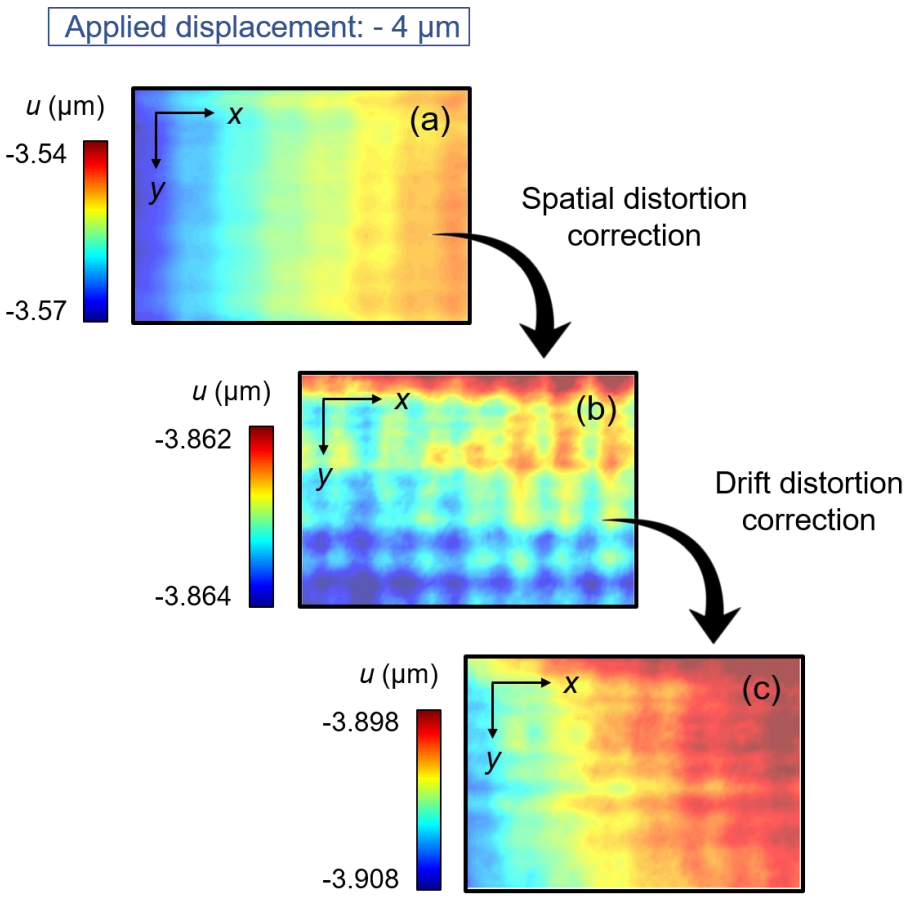
Applied displacement: - 4 µm
u (µm)
-3.54
-3.57
x
y
(a)
Spatial distortion correction
u (µm)
-3.862
-3.864
x
y
(b)
Drift distortion correction
u (µm)
-3.898
-3.908
x
y
(c)

Figure 8

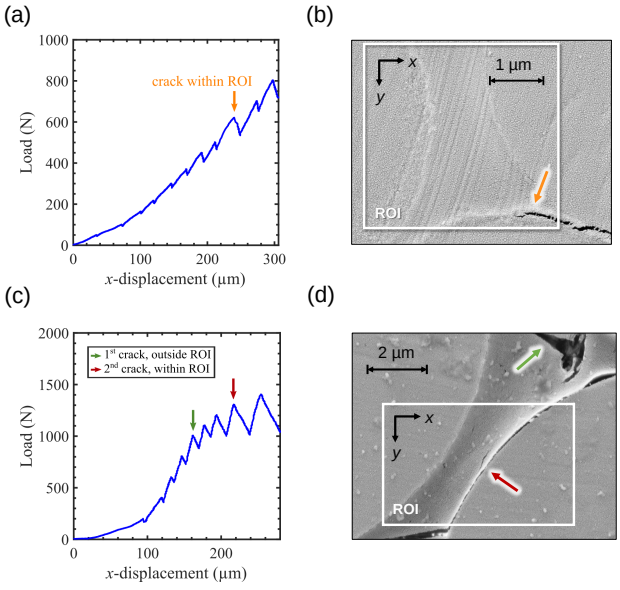
(a)
(b)
(c)
(d)
crack within ROI
Load (N)
x-displacement (μm)
1 μm
2 μm
ROI
x
y
1st crack, outside ROI
2nd crack, within ROI

Figure 9

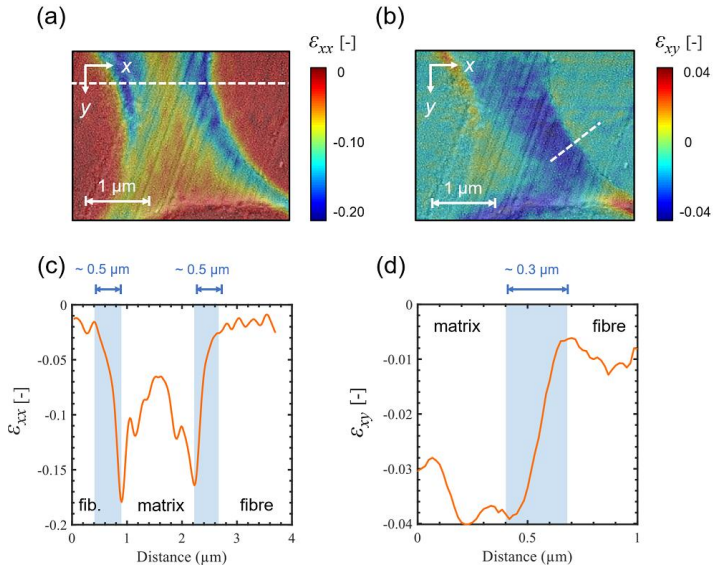
(a)
ε_{xx} [-]
0
-0.10
-0.20
x
y
1 µm
(b)
ε_{xy} [-]
0.04
0
-0.04
x
y
1 µm
(c)
~ 0.5 µm
~ 0.5 µm
ε_{xx} [-]
fib.
matrix
fibre
Distance (µm)
(d)
~ 0.3 µm
matrix
fibre
ε_{xy} [-]
Distance (µm)

Figure 10

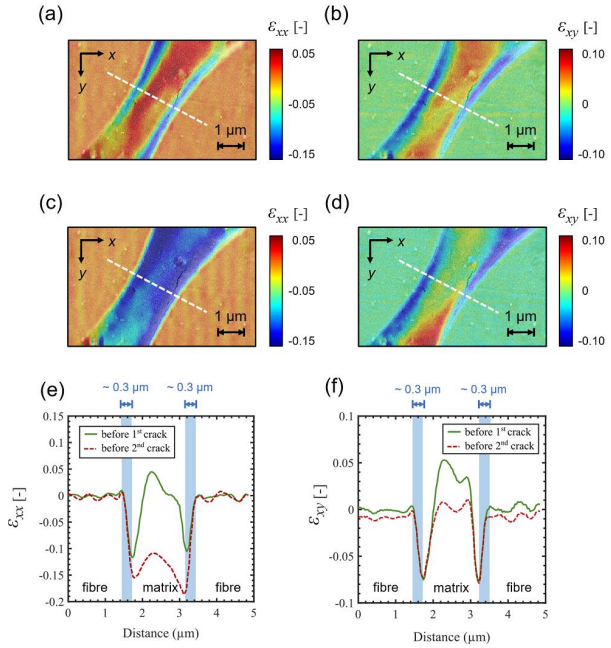
(a)
(b)
(c)
(d)
(e)
(f)
ε_{xx} [-]
ε_{xy} [-]
0.05
-0.05
-0.15
0.10
0
-0.10
x
y
1 µm
~ 0.3 µm
~ 0.3 µm
before 1st crack
before 2nd crack
fibre
matrix
fibre
Distance (µm)

Figure 11

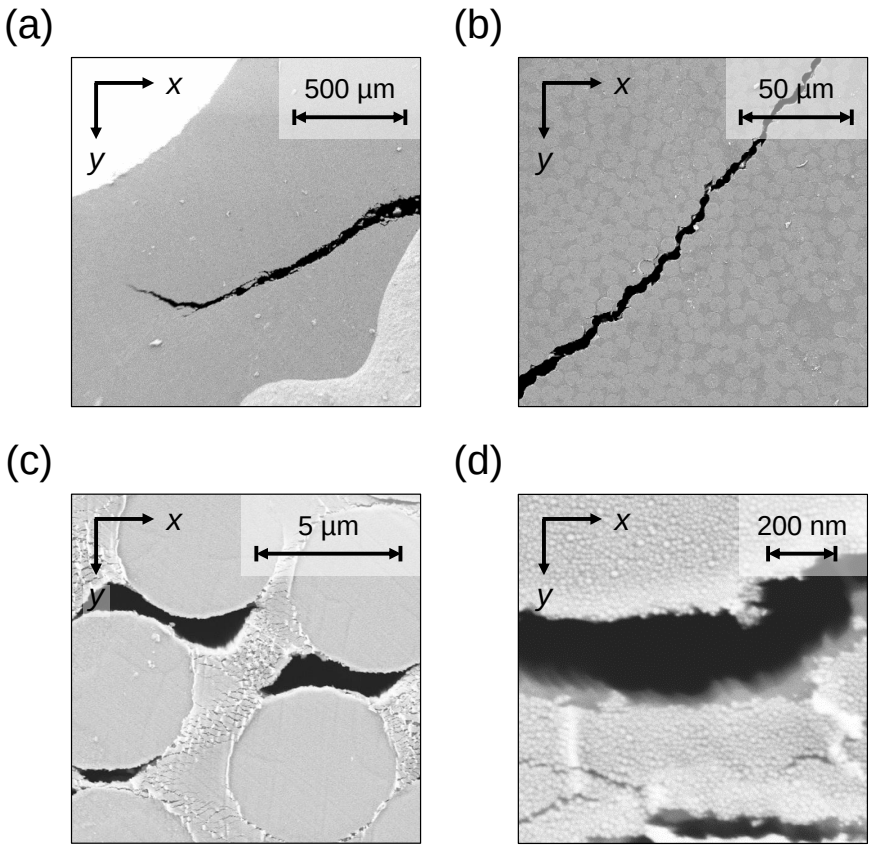

Figure 12

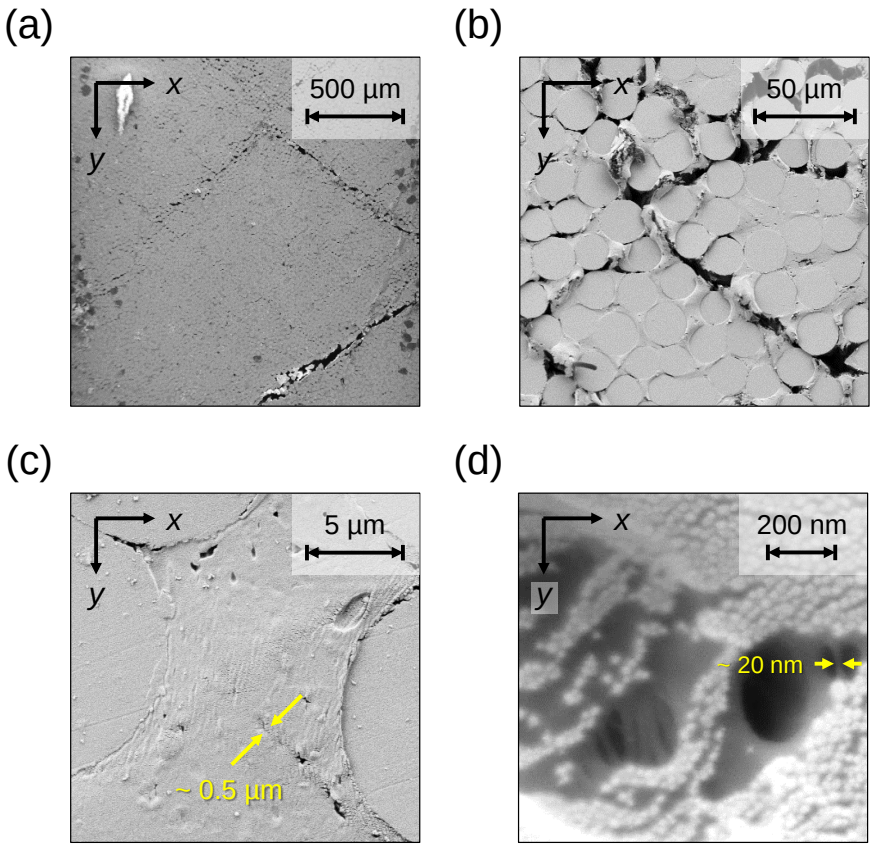

Figure 13

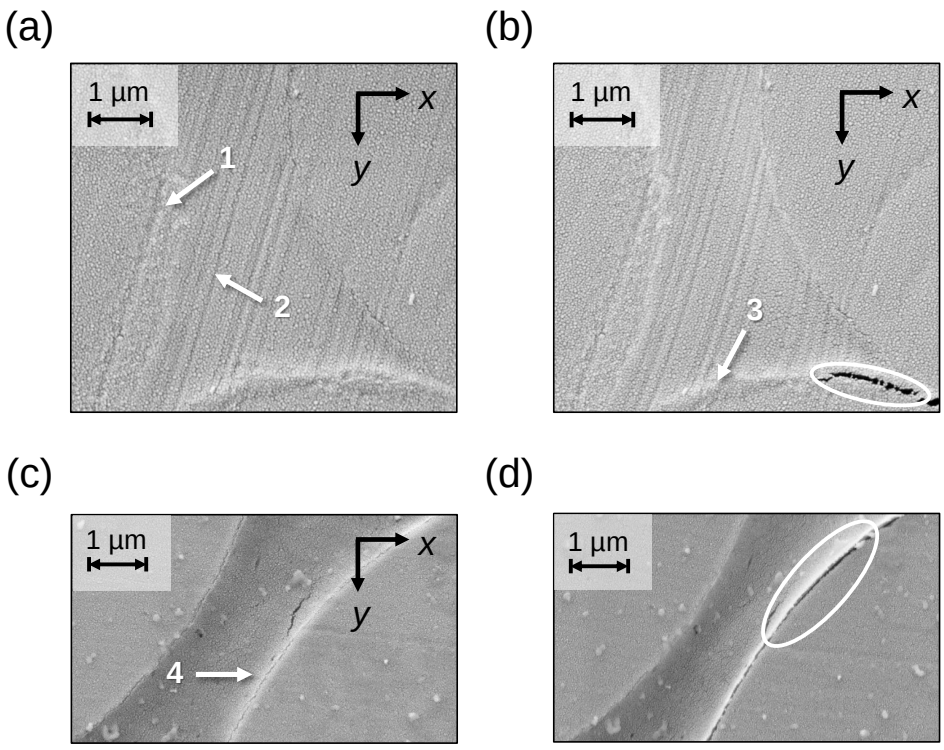

Figure 14

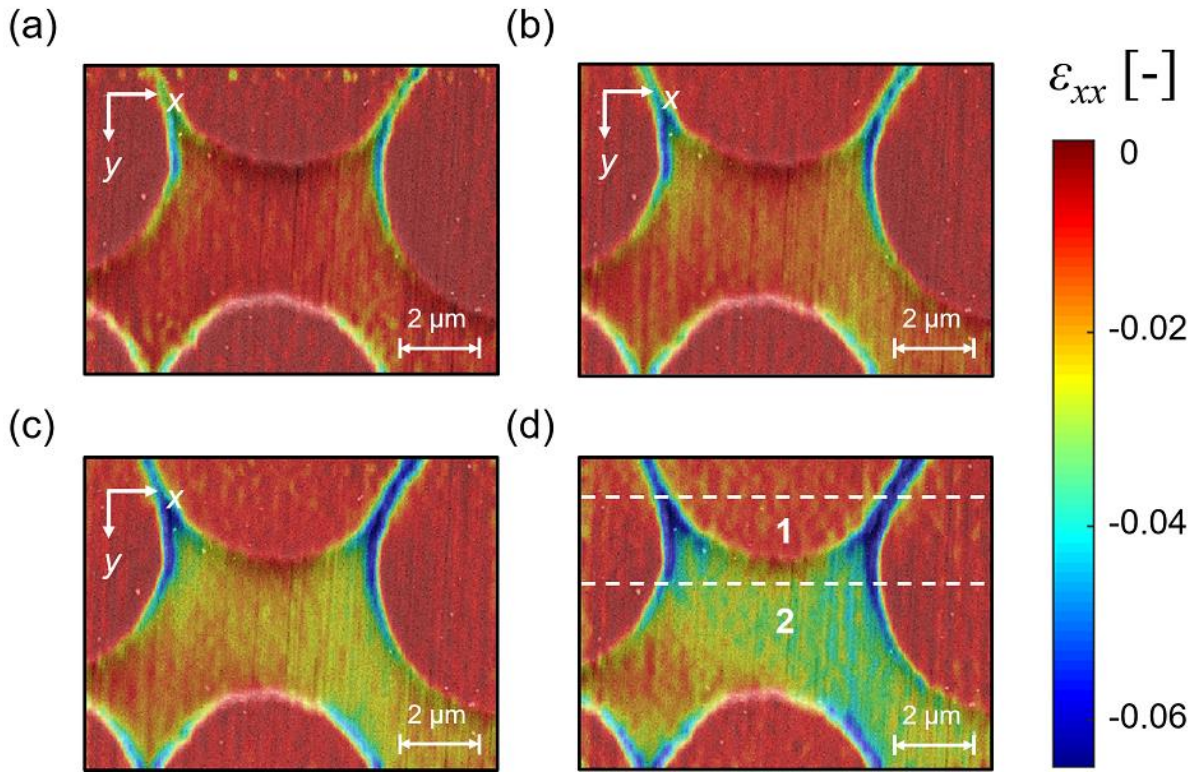

Figure 15

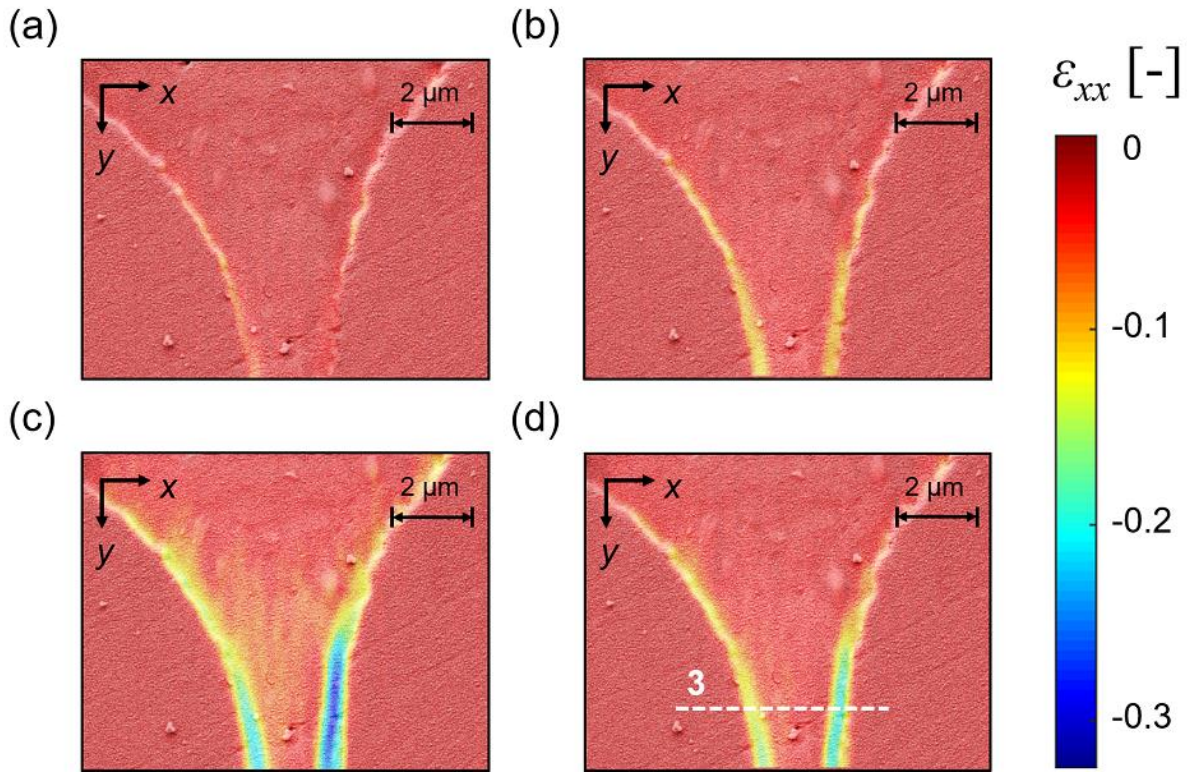

Figure 16

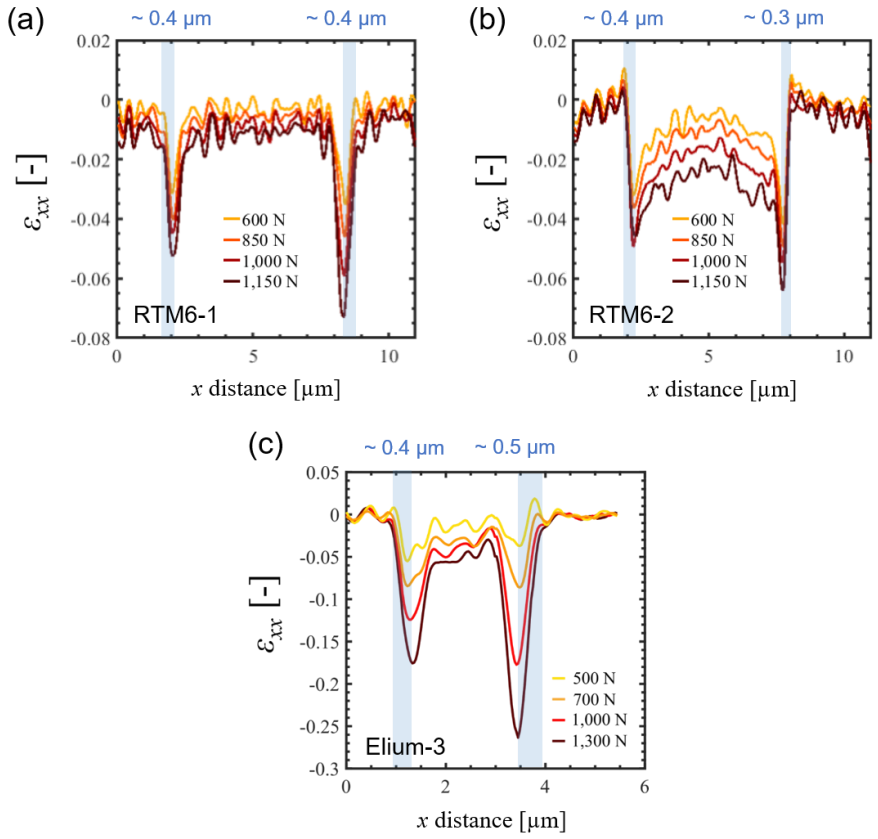
(a)
~ 0.4 µm
~ 0.4 µm
ε_{xx} [-]
600 N
850 N
1,000 N
1,150 N
RTM6-1
x distance [µm]
(b)
~ 0.4 µm
~ 0.3 µm
ε_{xx} [-]
600 N
850 N
1,000 N
1,150 N
RTM6-2
x distance [µm]
(c)
~ 0.4 µm
~ 0.5 µm
ε_{xx} [-]
500 N
700 N
1,000 N
1,300 N
Elium-3
x distance [µm]

Figure 17

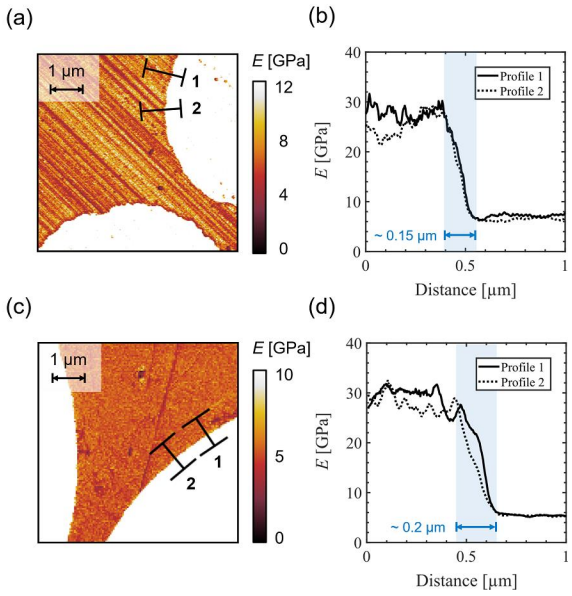
(a)
(b)
1 µm
1
2
E [GPa]
12
8
4
0
Profile 1
Profile 2
E [GPa]
40
30
20
10
0
~ 0.15 µm
0
0.5
1
Distance [µm]
(c)
(d)
1 µm
1
2
E [GPa]
10
5
0
Profile 1
Profile 2
E [GPa]
40
30
20
10
0
~ 0.2 µm
0
0.5
1
Distance [µm]

Figure 18

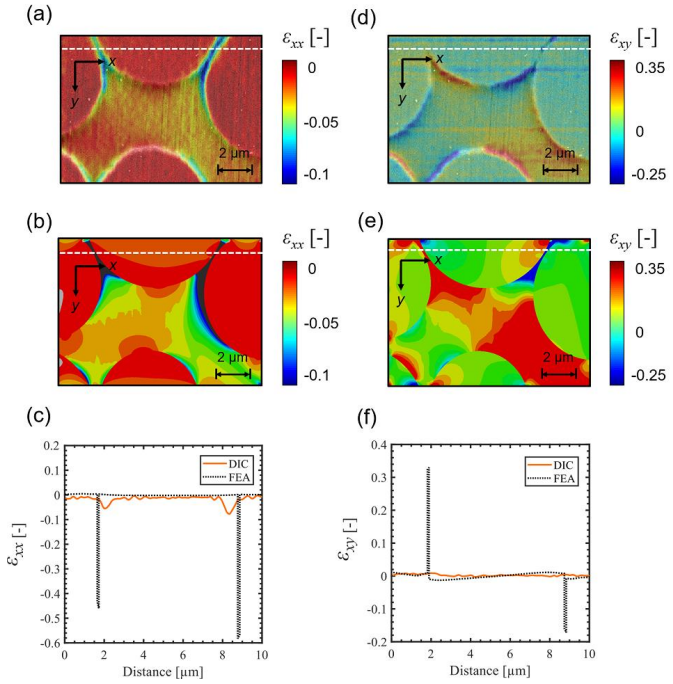
(a)
(b)
(c)
(d)
(e)
(f)
ε_{xx} [-]
ε_{xy} [-]
0
-0.05
-0.1
0.35
-0.25
x
y
2 µm
DIC
FEA
Distance [µm]

Figure 19

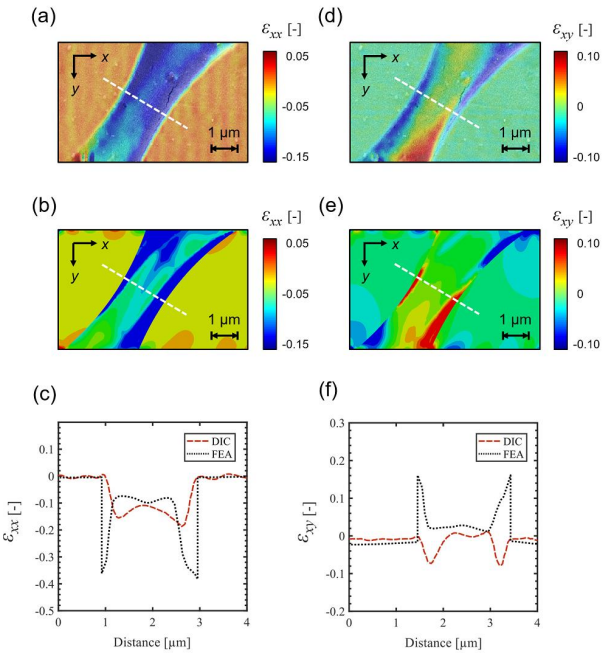
(a)
ε_{xx} [-]
0.05
-0.05
-0.15
x
y
1 µm
(d)
ε_{xy} [-]
0.10
0
-0.10
(b)
(e)
(c)
DIC
FEA
ε_{xx} [-]
Distance [µm]
(f)
ε_{xy} [-]

Figure 20

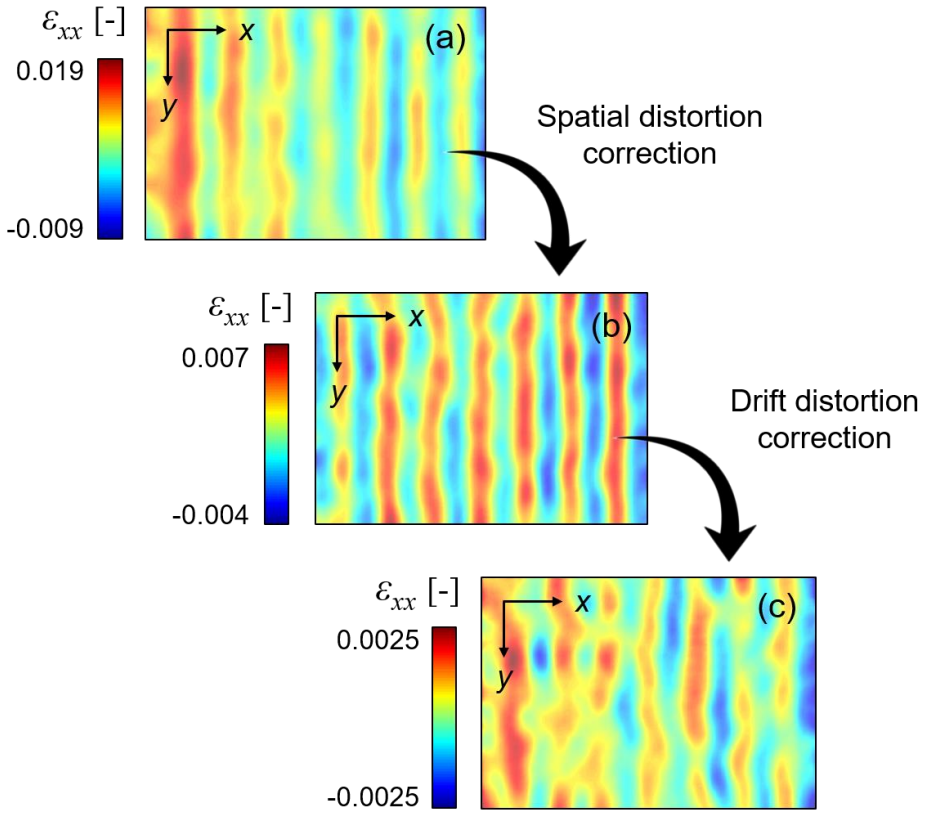
ε_{xx} [-]
0.019
-0.009
x
y
(a)
Spatial distortion correction
ε_{xx} [-]
0.007
-0.004
x
y
(b)
Drift distortion correction
ε_{xx} [-]
0.0025
-0.0025
x
y
(c)

Figure 21

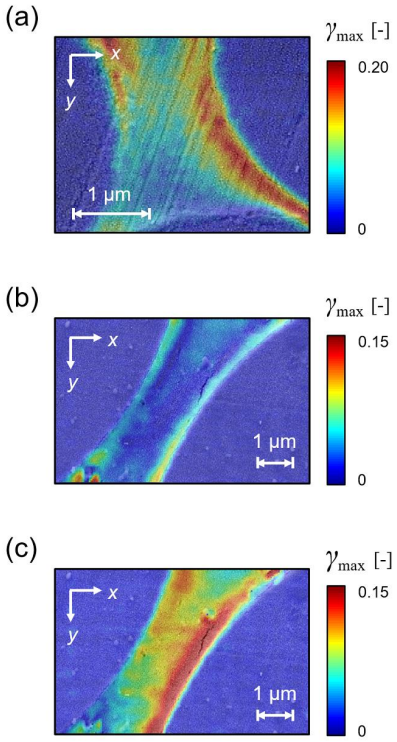
(a)
x
y
1 µm
γ_{max} [-]
0.20
0
(b)
x
y
1 µm
γ_{max} [-]
0.15
0
(c)
x
y
1 µm
γ_{max} [-]
0.15
0